



HAL
open science

Liquid cooling of a microprocessor: experimentation and simulation of a sub-millimeter channel heat exchanger

Julien Fontaine, Charles Gonzalez, Prashant Kumar, François Pigache, Pascal Lavieille, Frédéric Topin, Marc Miscevic

► To cite this version:

Julien Fontaine, Charles Gonzalez, Prashant Kumar, François Pigache, Pascal Lavieille, et al.. Liquid cooling of a microprocessor: experimentation and simulation of a sub-millimeter channel heat exchanger. Heat Transfer Engineering, 2019, 41 (15-16), pp.1365-1381. 10.1080/01457632.2019.1628485 . hal-03079615v3

HAL Id: hal-03079615

<https://hal.science/hal-03079615v3>

Submitted on 4 Feb 2022

HAL is a multi-disciplinary open access archive for the deposit and dissemination of scientific research documents, whether they are published or not. The documents may come from teaching and research institutions in France or abroad, or from public or private research centers.

L'archive ouverte pluridisciplinaire **HAL**, est destinée au dépôt et à la diffusion de documents scientifiques de niveau recherche, publiés ou non, émanant des établissements d'enseignement et de recherche français ou étrangers, des laboratoires publics ou privés.



Distributed under a Creative Commons Attribution - NonCommercial - NoDerivatives 4.0 International License

1 **Liquid Cooling of a Microprocessor: Experimentation and Simulation of a**
2 **Sub-Millimeter Channel Heat Exchanger**

3
4
5 **Fontaine J.¹, Gonzalez C.^{1,2}, Kumar P.², Pigache F.¹, Lavieille P.¹, Topin F.², Miscevic M.¹**

6
7
8 ¹University of Toulouse, LAPLACE (Laboratory on Plasma and Conversion of Energy), Toulouse, France

9 ²Aix Marseille Univ, CNRS, IUSTI, Marseille, France

10
11
12
13
14
15
16
17
18
19
20
21
22
23
24
25
26
27
28
29
30
31
32
33
34 Address correspondence to Dr. Marc Miscevic, University of Toulouse, LAPLACE, UPS-INP-
35 CNRS, 118 Route de Narbonne, 31062 Toulouse Cedex 09, France. E-mail:
36 marc.miscevic@laplace.univ-tlse.fr
37

1 **ABSTRACT**

2 *A heat exchanger dedicated to the cooling of a microprocessor has been designed and realized.*
3 *This heat exchanger consists of a bottom wall in contact with the processor and a cover that has*
4 *been dug to a depth of 200 μm on one side and 1 mm on the other side. Thus, by turning the*
5 *cover, the hydraulic diameter of the channel can be changed. Both hydraulic and thermal*
6 *performances of this heat exchanger have been experimentally tested. At the same time, 3D*
7 *numerical simulations were carried out on a model of the experimental prototype. Comparisons*
8 *between numerical and experimental results are in good agreement. In particular, the influence*
9 *of the distributor and the collector on the distribution of fluid flow and heat fluxes is emphasized.*
10 *A new concept of micro heat exchanger was then proposed for the cooling of electronics devices*
11 *for which wall to fluid heat exchange quality as well as pumping effect is very critical. In the*
12 *present work, the ability of a liquid heat exchanger involving a dynamic deformation of one of its*
13 *walls to cool a microprocessor is investigated. For that purpose, 3D transient numerical*
14 *simulations of fluid flow and conjugate heat transfer were performed using commercial software*
15 *based on the finite volume. Effect of geometrical and actuation parameters has been explored*
16 *demonstrating the ability of such heat exchanger to simultaneously pump the fluid and enhance*
17 *the heat transfer.*

18

1 ***INTRODUCTION***

2 The evacuation of the heat generated within a microprocessor is a crucial problem. It
3 affects the user from various points of view: limitation of performance and maximum allowable
4 temperature of the environment in which it can be used, drastic reduction in reliability and
5 lifetime, energy consumption of the chip. It is therefore necessary to develop efficient cooling
6 solutions even for high heat generation microprocessors and to keep it near its optimum operating
7 temperature. Numerous works have been conducted to propose new techniques to enhance heat
8 transfer and improve existing ones [1]. For application in high dissipative electronics, air-cooling
9 appears to be increasingly inappropriate due to low thermal conductivity as well as low density
10 and low heat capacity of this fluid. Thus, liquid or two-phase thermal management systems must
11 be developed. Furthermore, in addition to the rapid increase in the power density, electronic
12 packages are more and more miniaturized, implying to develop efficient cooling systems. Several
13 cooling solutions can then be envisaged. Among these solutions, micro channels-based heat
14 exchanger is often presented as one of promising cooling technologies [2-8]. For example, very
15 recently Kheirabadi and Groulx [8] have shown a device whose thermal resistance is varying
16 from 0.105 K/W to 0.08 K/W when the coolant (water) flowrate varies from 1.1 l/min to 3.8 l/min
17 in a microchannel heat sink in which channels were 0.5 mm wide and 2.3 mm tall.

18 Yang *et al.* [9] have proposed a general optimization process for the thermo-hydraulic
19 performances of mini-channel heat sinks. They reported empirical correlations extracted from
20 literature and gave some recommendations about their use for practical design. Although many
21 works have already been carried out, thermo-hydraulic behavior and performances of such
22 miniature heat sinks are still to be explored [10, 11].

23 Among these micro channel-cooling systems, those equipped with corrugated channels
24 appear particularly interesting. Heat transfer and pressure drop in sinusoidal corrugated channels

1 have been studied by Nishimura *et al.* [12]. These authors showed that transition between laminar
2 and turbulent flows is obtained at lower Reynolds number ($Re = 300$) compared to straight
3 channel due to unsteady vortex motion. As for flat channel, the friction factor is inversely
4 proportional to Reynolds number in the laminar flow range, while it is independent of Reynolds
5 number in the turbulent one. Extending this study, Nishimura *et al.* [13] studied flow patterns
6 characteristics in symmetrical two-dimensional sinusoidal and arc-shaped corrugated channels at
7 moderate Reynolds numbers ($20 < Re < 300$). They concluded that the transitional Reynolds
8 number depends on the corrugation shape and is lower for the arc-shaped wall.

9 Niceno and Nobile [14] have conducted an extended numerical study on these corrugated
10 channels. They found that these two corrugation shapes are ineffective in terms of heat transfer
11 rate (slightly higher for sinusoidal compare to arc-shaped channel) as compared to flat channel in
12 steady low Reynolds flow. The unsteady regimes appear at different Reynolds numbers for the
13 two corrugation shapes: unsteady regime was observed at $Re = 60 - 80$ for arc-shaped channel
14 and at $Re = 175 - 200$ for sinusoidal one. On the other hand, heat transfer rate increases
15 significantly for both corrugation shapes, up to a factor of three, as a result of self-sustained
16 oscillations. Moreover, this transfer rate was found to be higher for arc-shaped channel while the
17 friction factor was smaller for sinusoidal channel.

18 Naphon [15] conducted a numerical study on various corrugation geometries arranged in
19 in-phase and out-phase layouts (e.g. flat plate, arc-shaped, trapezoidal and V-shaped) to enhance
20 the thermal performances. He obtained that for a given air flow rate, V-shaped corrugated
21 channel enhances most heat transfer. This enhancement is linked to boundary layer disruption.
22 Most of the studies revealed an increase in overall thermal performance from 3 to 5 times
23 depending on the working fluid. However, static corrugated channels have shown to increase
24 significantly the pressure drop. In such corrugated (and grooved) mini-channels, high heat

1 transfer usually leads to high Reynolds number (mostly turbulent) flow.

2 Yang *et al.* [16, 17] compared three different designs of a micro heat exchanger for use in a
3 liquid cooling system. Best thermal performances were obtained with the chevron channel heat
4 exchanger. Unfortunately, this heat exchanger was also the one generating the highest pressure
5 drops.

6 On the other hand, Léal *et al.* [18] proposed a relatively simple model of dynamic
7 corrugated mini-channel to be operated at low Reynolds number. This has been achieved by
8 deforming dynamically one of the channel walls. Very high heat transfer has been obtained
9 compared to static corrugated channel (with a relative gain in heat transfer coefficient of about
10 400%). It appeared to be the first study to introduce dynamic wall in such mini-channels heat
11 exchanger.

12 Very recently, Kumar *et al.* [19] extended this work and proposed a realistic 3D geometry
13 of dynamic corrugated heat exchanger. In their study, the average height of the channel is fixed
14 while the minimum gap (distance between the lowest point of the deformed wall and the fixed
15 wall) varies as a function of the relative amplitude. Numerical studies have been conducted for a
16 channel outlet pressure greater than the inlet one and for an imposed frequency of 50 Hz . They
17 showed that heat transfer coefficient is proportional to wave amplitude and that such devices
18 possess self-pumping capacity. This system can operate with negligible pressure drop, or even
19 without an external pump.

20 The aim of this paper is to determine the ability of this type of actuated liquid heat
21 exchanger to cool a micro-electronic device. First, a reference (static) heat exchanger has been
22 studied, from both experimental and numerical point of view. A systematic numerical study was
23 then conducted considering a micro-heat exchanger using three actuators to deform dynamically
24 one of its walls to understand the impact of operating parameters in enhancing thermo-hydraulic

1 characteristics.

2

3 **REFERENCE HEAT EXCHANGER**

4 **Experimental setup**

5 The reference exchanger consists of two parts, the sole made of copper and the cover made
6 of aluminum. Two grooves are machined in the sole and communicate with the inlet and outlet
7 pipes (see Figure 1). An O-ring is placed at the periphery for sealing. The cover is a simple
8 parallelepiped plate that has been dug to a depth of $200\ \mu\text{m}$ on one face and $1\ \text{mm}$ on the other.
9 Thus, by turning the cover, the hydraulic diameter of the channel can be changed. The channel
10 obtained for the circulation of the fluid after assembly is thus rectangular with a cross-section of
11 $50\ \text{mm}$ in width, $38\ \text{mm}$ in length (distance between the distributor and the collector) and is 200
12 μm or $1\ \text{mm}$ in height (Figure 2).

13 In order to be able to determine the thermal performance independently of the thermal
14 contact resistance between the exchanger and the microprocessor, three thermocouples were
15 inserted into the sole at a distance of $1\ \text{mm}$ from the surface in contact with the liquid. These
16 thermocouples are K-type, sheathed in stainless steel, $500\ \mu\text{m}$ in diameter. The holes in the sole
17 were made by electro erosion; they have a diameter of $600\ \mu\text{m}$ and a length of $33\ \text{mm}$. Two other
18 identical thermocouples are placed in inlet and outlet pipes along with pressure taps (diameter 4
19 mm) in order to measure the inlet and outlet bulk temperatures of the fluid. All thermocouples
20 have been calibrated against a certified Pt100 RTD probe (accuracy of $0.05\ ^\circ\text{C}$). Thus, the
21 relative accuracy of temperature measurements is estimated at $0.1\ ^\circ\text{C}$. A differential pressure
22 sensor is positioned between the inlet and outlet pipes of the heat exchanger (the connections are
23 located $25\ \text{cm}$ upstream and downstream of the heat exchanger) and allows measuring the
24 pressure loss with an accuracy better than $10\ \text{Pa}$.

1 The heat source is constituted by a microprocessor mock-up supplied by Intel Company
2 and fixed to the sole. This mock-up is geometrically identical to a commercially available
3 processor and generates similar and easily scalable thermal solicitations.

4 The heat exchanger is connected to a hydraulic circuit (see schema in Figure 3). A counter-
5 current tubular heat exchanger is used as cold source for the fluid loop. The fluid then passes
6 through a Coriolis flowmeter allowing mass flow rate measurements in the range 0 up to 6 g/s
7 with an accuracy of 0.02 g/s. We thus obtained a maximum Reynolds number of 240 within the
8 heat exchanger for both considered thicknesses (hydraulic diameter respectively equal to 1960
9 μm and 398 μm). A variable speed gear pump is used for discharging the fluid into a precision
10 valve. This latter allows us to vary the pressure drop in the circuit at the desired value in a simple
11 manner. The fluid then flows toward the inlet of the heat exchanger prototype. A reservoir (open
12 to the atmosphere) is connected to the hydraulic circuit and serves as an expansion vessel. The
13 secondary fluid in this heat exchanger is thermostated water.

14

15 **Numerical simulation**

16 Simultaneously, direct numerical simulations of this heat exchanger were carried out using
17 commercial software Star- CCM+. The virtual prototype was constructed using the CAD model
18 of the assembly (bottom wall, top cover and channel). The conjugate heat transfer problem was
19 solved in the transient regime, and heat conduction is considered in all solid parts. Note that a
20 perfect thermal contact between top and bottom parts of the assembly was considered. For the
21 channel as well as inlet and outlet manifolds, incompressible laminar and transient flow and heat
22 transfer were solved using the classical combination of continuity, momentum and energy
23 equations (here simply written for constant properties):

$$24 \quad \vec{\nabla} \cdot \vec{u} = 0 \quad (1)$$

1
$$\rho \frac{\partial \vec{u}}{\partial t} + \rho(\vec{u} \cdot \vec{\nabla})\vec{u} = \rho \vec{g} - \vec{\nabla} \cdot \vec{P} + \mu \Delta \vec{u} \quad (2)$$

2
$$\rho C_p \left(\frac{\partial T}{\partial t} + \vec{u} \cdot \vec{\nabla} T \right) + \rho \vec{u} \cdot \frac{\partial \vec{u}}{\partial t} + \frac{\rho}{2} (\vec{\nabla} \|\vec{u}\|^2) \cdot \vec{u} = k_f \Delta T + \frac{\partial P}{\partial t} + \Phi \quad (3)$$

3 Where Φ is the volumetric energy source due to viscous dissipations. This term is taken into
 4 account during all calculations; however, in the present work, it is negligible compared to the
 5 wall heat transfer.

6 The physical properties of the fluid were considered to vary with the temperature (water
 7 using the models of IAPWS-IF97 (International Association for the Properties of Water and
 8 Steam, Industrial Formulation 1997) while the solid part properties are supposed constant (copper
 9 for the base and aluminum for the top cover). The numerical resolution used a segregated
 10 approach with implicit second order temporal discretization and ad hoc relaxations factors in
 11 order to obtain adequate convergence behavior. $1\ 691\ 272$ and $1\ 852\ 205$ meshes were used for
 12 the $1\ mm$ and the $200\ \mu m$ heat exchanger, respectively. For both cases, an unstructured trimmer -
 13 octree mesh type- is used in solid parts while structured hexahedral anisotropic cells are used in
 14 the channel with 16 up to 20 cells along the height of the channel. This mesh is refined in the
 15 vicinity of all solid-fluid interfaces and near inlet and outlet of the channel. Mesh convergence
 16 effects were checked, and no additional improvement is obtained with further refinement.

17 Both mass flow rate and fluid temperature were imposed at the inlet of the heat exchanger;
 18 outlet pressure is imposed at the atmospheric one. A uniform heat flux is imposed on the bottom
 19 wall of the sole, on an area of $30 \times 30\ mm^2$ as in the experiments. The rest of the solid walls are
 20 considered adiabatic (as experimental results show that thermal losses are negligible).

21

22 ***NUMERICAL ACTUATED PROTOTYPE***

23 In the studied configuration, the lower wall was fixed and subjected to a constant heat flux

1 along the imprint of heating zone while the dynamically deformed upper wall (also called
2 "membrane" in the following) and side walls were kept adiabatic. Several actuators were
3 employed to dynamically deform the upper wall of a rectangular cross section micro-channel in
4 order to simultaneously enhance heat transfer and pump the fluid.

5 The length of the actuated zone (L) is 49 mm while width (W) is 35 mm . The channel gap
6 (g) is fixed and is $10\text{ }\mu\text{m}$ while the average height of the channel (δ) is linked to the wave
7 amplitude employed for wall deformation and the channel gap. The lengths of input and outlet
8 zones have been chosen long enough to establish the hydrodynamic. Furthermore, the no-slip
9 condition was imposed on the walls.

10 The influences of relative amplitude (A_0), frequency (f_r) and wavelength (λ) on thermo-
11 hydraulic performances are studied for an imposed value of the pressure difference between
12 outlet and inlet of the exchanger equal to zero.

13 Only three actuators were employed in the present study. The channel cross-section shape
14 is presented on Figure 4 where the actuator positions can be described using x_1, x_2, x_3, x_4, x_5 and
15 x_6 . The positions x_0 and x_7 are fixed to external inlet and outlet zones as dampers. These small
16 zones make the fluid to enter and leave in laminar condition. The micro-channel geometry is
17 composed of four main parts: inlet zone, heated surface where the heat power is imposed, outlet
18 zone and membrane. This simplified geometrical configuration, dedicated to study the impact of
19 actuators operating parameters (3 actuators case) do include sidewall-damping effects on the
20 lateral side of the actuated zone. Along main flow axis the membrane displacement is linearly
21 interpolated between actuators pair and between actuator and fixed zone.

22 3D numerical simulations were carried out using the commercial software StarCCM+. This
23 software allows modeling fluid flow and heat transfer in dynamically deformed structures. The
24 flow was considered transient, three-dimensional and laminar. The working fluid was liquid

1 water (properties taken from IAPWS-97 at 27 °C) whose all thermo-physical properties were
2 supposed constant for systematic studies. The imposed heat power on the imprint (heated zone)
3 was 65 W (note that only half of the device is modeled due to symmetry).

4 The results presented focus on the "active zone" namely between S_1 and S_2 sections (see
5 Figure 4). All representative global thermo-hydraulic quantities were calculated in this zone.

6 The incompressible laminar and transient conjugate flow and heat transfer problems were
7 solved as for the static heat exchanger. The numerical resolution used a segregated approach with
8 implicit second order temporal discretization and ad hoc relaxations factors in order to obtain
9 adequate convergence behavior. The displacement of the top membrane is created by:

- 10 (1)- fixing it in inlet and outlet zone and displacing the upper wall at chosen height δ
11 (average height of the channel),
- 12 (2)- adding the movement of the three actuators (Eq. 4),
- 13 (3)- in between two actuators or one actuator and border, the displacement is simply
14 interpolated.

15 The displacement of actuator is given by the following equation for $i=1,2,3$ corresponding
16 to actuator along main flow axis:

$$17 \quad Act_i(x, t) = A_o \cdot \cos(2\pi f_r t + \Phi_i) \quad (4)$$

18 where $\Phi_1 = 0^\circ, \Phi_2, \Phi_3$ are phase of actuators Act_1, Act_2 and Act_3 , respectively.

19 In the studied configuration, the vertical plane passing through the central axis of the
20 channel is a plane of symmetry, so only half of the channel was simulated (i.e. $W/2=17.5 \text{ mm}$).
21 The imposed power on the modeled half-imprint was thus 32.5 W to carry out numerical
22 simulations (see Figures 4 and 5). This allows us to reduce the number of mesh cells to optimize
23 computation time by dividing the simulated configuration by two compared to its actual size.
24 Note that the fluid flow was considered in x-direction while the width and height of the channel

1 were considered in y- and z-directions, respectively.

2 Meshing strategy was similar to the one used by Kumar *et al.* [19]. It was rather tricky to
3 create a convenient mesh in such highly anisotropic geometrical configuration subjected to large
4 amplitude deformations (up to 98 % of channel height) while keeping a computational time low
5 enough to carry out parametric study without sacrificing precision or convergence of the dynamic
6 transfer.

7 The deformed channel mesh is presented in Figure 5 in case of an actuator size of 11 mm
8 and a phase-shift between two consecutive actuators of 120° ($\Phi=0^\circ, -120^\circ, -240^\circ$).

9 In case of dynamic corrugated channel, surface averaged and volume averaged thermo-
10 hydraulic quantities for all operating configurations were calculated as follow. The Reynolds
11 number and hydraulic diameter are defined by:

$$12 \quad Re = \frac{\rho \|\bar{u}\| D_h}{\mu}, D_h = \frac{1}{\lambda} \int_0^\lambda \frac{4S}{p} d\lambda \quad (5)$$

13 Where S is the flow fluid passage area along the heated zone and p is the perimeter of the
14 passage section, respectively. Note that these quantities are averaged over a time period.

15 Following the method used in Léal *et al.* [18], the heat transfer coefficient is obtained by the
16 spatial and temporal averaged fluid temperature and wall temperature over the width and between
17 sections S_1 and S_2 (distance L) as well as over a period ($\tau=1/f_r$):

$$18 \quad \bar{T}_w = \frac{1}{\tau WL} \int_t^{t+\tau} \int_{S_1}^{S_2} \int_0^W T_w(x, y, t) dx dy dt \quad (6)$$

$$19 \quad \bar{T}_{mf} = \frac{1}{\tau \delta WL} \int_t^{t+\tau} \int_{S_1}^{S_2} \int_0^{z(x,t)} \int_0^W T_{mf}(x, y, z, t) dx dy dz dt \quad (7)$$

20 In the following, the global heat transfer coefficient and Nusselt number across the channel
21 (between S1 and S2) are defined as:

$$22 \quad \langle h \rangle = \frac{\Gamma}{(\bar{T}_w - \bar{T}_{mf})}, \langle Nu \rangle = \frac{\langle h \rangle D_h}{k_f} \quad (8)$$

1 The calculations to test mesh convergence were performed for amplitude $A_0 = 85 \mu m$ and
2 frequency $f_r = 20 Hz$. We initialized both corrugated shape and fluid flow. Then, calculations
3 were carried out until a periodic stationary regime is reached. This latter point is checked
4 comparing the temporal evolutions of global heat transfer and flow characteristics: calculations
5 were performed until the heat transfer coefficient values between two consecutive time periods
6 differs by less than 1 %. Consequently, an additional time period is added to extract all
7 instantaneous and time-averaged values of all physical quantities.

8 From the Table 1, it can be seen that reducing the characteristic mesh size from 3 to 2 mm
9 does not impact strongly on the global properties. The percentage differences between the
10 properties are respectively: 0.14 % for \dot{m} , 0.0024 % for T_w , 0.006 % for T_{mf} , 0.47 % for $\langle h \rangle$,
11 0.0095 % for T_{fi} and 0.0095 % for T_{fo} . On increasing the mesh size, these quantities vary
12 significantly while reducing it further do not lead to any additional improvement. Based on these
13 observations and the percentage difference in the properties, we chose the BMS (Base Mesh Size)
14 equal to 2 mm to perform the systematic studies.

15 To perform the numerical simulations in terms of time effectiveness as well as the
16 precision, it is very important to obtain an optimized time step (TS). We test the following
17 number of time steps per period: 20, 50, 75 and 100. Based on these time steps, global
18 characteristics have been presented in Table 2. It can be observed that heat transfer coefficient
19 values decrease with increase in TS . On the other hand, $\Delta T_m = T_w - T_{mf}$ increases with increase in
20 TS .

21 In order to obtain an optimized TS value, we have calculated the percentage variation of
22 $\langle h \rangle$ and ΔT_m for different time steps based on the lowest value as a reference value for both
23 these quantities. When $TS=50$, we observed a variation of $\langle h \rangle$ equal to 2.84 % while the
24 variation in ΔT_m is 6.14 %. The global results of different characteristics do not vary strongly

1 when increasing TS . Moreover, higher value of TS increases the computational time while the
2 properties vary within a difference of 3 %. Hence, $TS=50$ has been chosen to study the impact of
3 different amplitudes and frequencies.

4

5

6 **HYDRAULIC RESULTS**

7 **Hydraulic behavior of the reference heat exchanger**

8 A first series of experimental tests and numerical simulations were carried out without
9 powering the processor, at a temperature of $20\text{ }^{\circ}\text{C}$, in order to characterize the heat exchanger
10 from hydraulic point of view. The pressure losses obtained as a function of the mass flow rate are
11 reported in Figure 6 for the two considered channel thicknesses ($200\text{ }\mu\text{m}$ and 1 mm). Globally,
12 experiments and numerical simulations exhibit the same trend. Nevertheless, significant
13 discrepancies are found between experimental and numerical results, especially for the 1 mm
14 channel. These discrepancies can be explained by the fact that the pressure losses in the
15 numerical simulations are determined between the inlet and the outlet of the heat exchanger,
16 while in the experiments the tapings for the pressure measurement are located at 25 cm upstream
17 and 25 cm downstream of the prototype. Thus, additional pressure losses are taken into account in
18 the experiments (regular pressure drop in the inlet and outlet tubes, as well as singular pressure
19 drops in the connections between the tubes of the loop and the heat exchanger).

20 Furthermore, in the 1 mm channel heat exchanger, the flow distribution appears less
21 homogeneous than in the $200\text{ }\mu\text{m}$ channel heat exchanger, as it can be seen in Figures 7 and 8,
22 respectively. Such a flow maldistribution variation according to the channel hydraulic diameter is
23 not surprising: it has widely been highlighted. For example, Kheirabadi and Groulx [4]
24 numerically calculated variation of the mean velocity from a channel to another in an array of

1 parallel microchannels connected to a single manifold at the inlet and at the outlet. Variation up
 2 to 52 % was highlighted for the 1 mm microchannel width, while this variation was only 16 % for
 3 the 0.25 mm microchannel width. In the present study, the flow distribution in the 1 mm channel
 4 heat exchanger could be homogenized by optimizing the distributor and collector headers as
 5 suggested, for instance, by Saeed and Kim [20]. From these figures, it can be speculated that the
 6 main part of the pressure drop in the 200 μm channel heat exchanger is the regular pressure drop
 7 in the channel itself, while in the 1 mm the main part of the pressure drop corresponds to the
 8 pressure drop in the singularities and in the manifolds.

9 To assess the respective contributions of the channel and the singularities on the total
 10 pressure drop, an analytical estimation can be done. Assuming a Poiseuille flow in the inlet and
 11 outlet tubes, as well as in the channel, the pressure drop can be calculated as:

$$12 \quad \Delta p = \frac{64}{Re_{D_t}} \frac{L_t}{D_t} \frac{1}{2} \rho U_t^2 + \frac{64}{Re_{D_h}} \frac{L_c}{D_h} \frac{1}{2} \rho U_c^2 + \sum_i \xi_i \frac{1}{2} \rho U_c^2 \quad (10)$$

13 With:

$$14 \quad Re_{D_t} = \frac{\rho U_t D_t}{\mu}, Re_{D_h} = \frac{\rho U_c D_h}{\mu} \quad \text{with} \quad D_h = \frac{4el}{2(e+l)} \approx 2e$$

15 The last term in equation 10 represents the pressure drop due to all the singularities. The
 16 value of $\sum_i \xi_i$ is adjusted to reproduce the experimental pressure drop of the 1 mm channel heat
 17 exchanger: $\sum_i \xi_i \approx 5$.

18 The global pressure losses of the device equipped with the 200 μm channel heat exchanger
 19 are 2 to 2.5 times higher than those measured with the one using the 1 mm channel heat
 20 exchanger, while the hydraulic diameter is 5 times lower. This behavior can be explained by
 21 analyzing the part of the regular pressure losses in comparison with the singular pressure losses
 22 corresponding to the different changes in flow direction and cross-sections. These relative
 23 contributions are shown in Figure 10. For the 1 mm channel heat exchanger, the pressure losses in

1 the actual channel are negligible, less than 2 % of the total pressure losses. For the 200 μm
2 channel, these pressure losses in the channel become preponderant and represent 60 to 70 % of
3 the total pressure losses. The superimposed graph on Figure 10 compare the numerical pressure
4 drop along each minichannel with the theoretical values deduced from established Poiseuille flow
5 model. A fair agreement is obtained in both case, the numerical value being globally about 10 %
6 higher than the theoretical one, this is due to the inlet-outlet effect along with maldistribution.

7

8 **Hydraulic behavior of the virtual dynamic prototype**

9 Local fields are presented for the dynamic heat exchanger with $A_0 = 100 \mu m$ and $f_r = 10 Hz$
10 for arbitrary time during periodic stationary regime. During expansion of the dynamic channel,
11 the fluid moves in the longitudinal direction because of the successive expansion and
12 contractions. Wall movement induces also vertical (i.e. towards heated wall) displacement of the
13 fluid. Characteristic times associated to vertical and horizontal fluid displacement are similar and
14 significantly lower than the actuation one.

15 Mass flow rate is proportional to both frequency and amplitude. High frequency leads to
16 fast movement of the corrugated wall, which in turn enhances the mass flow. The latter is
17 therefore directly proportional to the frequency (Figure 12 top). Increasing amplitude (at constant
18 gap) leads to increase the channel volume thus to have more fluid in the channel. This behavior
19 also enhances mass flow rate in the system, which is also directly proportional to the amplitude
20 (Figure 12 bottom). Note that increasing amplitude at constant gap adds mainly volume to the
21 channel near the membrane and increases average height.

22 Influence of gap size has been tested on mass flow rate and heat transfer for amplitude 100
23 μm and frequency 10 Hz. The initial gap was fixed at 10 μm and then varied up to 35 μm . On
24 Figure 13, it can be easily observed that mass flow rate decreases with increasing gap. This

1 indicates that global efficiency of such device is largely affected by the minimum constriction
2 height.

3

4 **THERMAL PERFORMANCE**

5 **Reference heat exchanger**

6 In order to determine the heat performance of the two configurations of the heat exchanger,
7 specific tests were carried out. The experimental protocol consists in imposing a water flow rate
8 by means of the gear pump and then supplying the microprocessor simulator with an electrical
9 power such that the water temperature difference between the inlet and the outlet is equal to
10 10 ± 0.2 °C. The inlet temperature of the water in the exchanger is imposed at 23.5 °C for all the
11 tests. The deviations between the applied electric power and the heat flux received by the water
12 (quantified by multiplying the mass flow rate with the enthalpy variation) vary between 0 and 7
13 % and are on average 4 %.

14 The mean temperature $\langle T_w \rangle$ of the bottom wall of the heat exchanger is evaluated by
15 performing a 2nd order polynomial regression of the measured wall temperatures and then
16 integrating this regression between the inlet and the outlet of the channel (i.e. between the outlet
17 of the distributor and the inlet of the collector, on a distance of 38 mm). It should be noted that
18 this calculation represents only an estimation of the mean temperature because it does not take
19 into account the 2D distribution of the surface temperature (variation in the direction
20 perpendicular to the main axis of the flow). The average fluid temperature $\langle T_f \rangle$ is estimated by
21 performing an arithmetic mean between the inlet and outlet water bulk temperatures. Considering
22 the operating conditions described above, this average temperature of the water in the heat
23 exchanger is substantially constant for all the experiments and is equal to 28.5 °C. An "apparent"

1 overall thermal conductance G of the heat exchanger is then defined as:

$$2 \quad G = \frac{\dot{m}c_p(T_{out}-T_{in})}{\langle T_w \rangle - \langle T_f \rangle} \quad (11)$$

3 The variations of this apparent overall thermal conductance as a function of the mass flow
4 rate are shown in Figure 14 for both considered channel thickness.

5 As it can be seen from this figure, the thermal conductance of the $200 \mu m$ channel heat
6 exchanger is substantially higher than that of the $1 mm$ one: enhancement up to 70 % is achieved
7 for mass flow rate approximately equal to 3 g/s. For such a mass flow rate, the overall thermal
8 conductance of the $200 \mu m$ channel heat exchanger is almost 15 W/K.

9 Let's consider 3 typical application cases using water as the working fluid, and a maximum
10 allowable fluid temperature difference of $10 \text{ }^\circ\text{C}$ between inlet and outlet. The severe environment
11 case will impose a cold source at a temperature relatively close to the maximum allowable
12 processor temperature (e.g. $70 \text{ }^\circ\text{C}$) along with limitations on the flowrate. In such conditions, heat
13 flux up to 125 W can be removed from the microprocessor with a mass flowrate of 3 g/s. The
14 temperature of the bottom wall of the heat exchanger would be only about $8 \text{ }^\circ\text{C}$ higher than the
15 fluid mean temperature. For a mass flow rate of about 5.4 g/s up to 225 W could be removed with
16 a wall to fluid temperature difference of less than $20 \text{ }^\circ\text{C}$ (e.g. automotive applications). Finally,
17 increasing the mass flow rate up to 9 g/s, the actuated channel allows to extract 375 W with a wall
18 to fluid temperature of $30 \text{ }^\circ\text{C}$. This device is thus also an efficient solution for data center type
19 applications. Moreover, contrarily to static mini/microchannels which generate prohibitory high
20 pressure drop and fluid maldistributions when operated in parallel, the active heat exchanger -due
21 to the pumping effect- constitute a best suited device for low pressure losses and well-distributed
22 flow in parallel branches of a fluid network. It can thus be concluded that such a heat sink can be
23 efficiently integrated to the different constraints of applications involving microprocessor thermal

1 management.

2 Numerical simulations have been performed in the same conditions than the experiments
3 (i.e. inlet water temperature equal to $23.5\text{ }^{\circ}\text{C}$, heat flux adjusted to obtain a temperature
4 difference between inlet and outlet of $10\text{ }^{\circ}\text{C}$). Virtual temperature sensors are placed at the same
5 locations than the experimental ones and data are extracted from the numerical temperature field.
6 The same procedure than - used in the experiments is then applied to calculate the apparent
7 overall thermal conductance; numerical results are reported along with experimental ones (Figure
8 14).

9 Adequacy between experimental and numerical results is excellent for the $200\text{ }\mu\text{m}$ channel
10 heat exchanger, while the numerical simulations slightly overestimate the overall thermal
11 conductance in the case of the 1 mm channel heat exchanger. As mentioned in the hydraulic
12 behavior section, the flow in the 1 mm channel is non-uniformly distributed. This maldistribution
13 of the flow implies that the temperature field of the fluid is farther from a one-dimensional field
14 than in the case of the $200\text{ }\mu\text{m}$ channel (see Figures 15 and 16). Calculating the mean temperature
15 of the fluid by integrating a second order polynomial trend curve as described above is therefore
16 less precise in the case of the 1 mm channel than in the case of the $200\text{ }\mu\text{m}$ channel. In the case of
17 the 1 mm channel heat exchanger, the flow field is more sensitive to the deviation in the imposed
18 inlet conditions and geometry compared to the real ones. It is thus not surprising to obtain a better
19 match between numerical results and experiments in the case of the best-distributed flow.

20

21 **Numerical prototype**

22 Due to movement of the channel wall, cold fluid is moved near the heated wall successively
23 at every location; this boundary layer disruption increases sharply heat transfer along with mixing

1 that takes place within the core flow. On temperature field, successive hot and “cold” plumes”
2 could be seen (Figure 17). Near inlet cold fluid fill the pocket during expansion, then is driven
3 toward heated surface, and eventually transferred below the next actuated zone. The constricted
4 zone acts as a barrier separating inlet and outlet parts. This leads the fluid to fill expansion zone
5 while being mixed efficiently; it is then transferred in the next pocket over time. These ”bursts”
6 repeat cyclically along with mixing thus increasing heat transfer.

7 Heat transfer coefficient depends on both imposed frequency and amplitude. Increasing
8 frequency increases the mixing effect and the fluid velocity. Thus, it results in high heat transfer
9 coefficients varying roughly proportionally to the frequency (see Figure 18.a). On the other hand,
10 increasing amplitude -while keeping the gap (minimum height below actuators) constant- leads to
11 increase the average height of the channel and thus reduces the heat transfer coefficient. This one
12 is thus found to decrease linearly with the amplitude (see Figure 18.b). Nevertheless, the heat
13 transfer coefficient remains very high (greater than $10\ 000\ W/m^2K$) for all tested cases. This is
14 due two main effects: the average fluid thickness increases, and the fluid velocities decrease.
15 Mainly the most constricted zones become less and less efficient as the gap increases. As these
16 zone (which cross all the channel length) are the place where the most efficient heat transfer takes
17 place, it is not surprising to observe a net decrease in heat transfer coefficient. Two main
18 conclusions could be drawn from these results: although the heat transfer coefficient decreases
19 when increasing channel height, for sub-millimeter cases it remains high enough to produce a
20 very small thermal resistance compared to the other involved in a chip cooling assembly (e.g.
21 contact resistances...). As, the flow increases with channel height, the need to remove relatively
22 high power with limited inlet-outlet temperature difference will by a more important design
23 parameter. Moreover, required pumping power and mechanical effort and constraints will be
24 more easily meet for channel with ”large” dimensions i.e. going more toward one millimeter than

1 *100 μm.*

2 A global thermal conductance of the virtual prototype can be derived from these heat
3 transfer coefficient values. The variation of this conductance is reported on Figure 19 along with
4 the experimental ones of the reference heat exchanger for both *1 mm* and *200 μm* channel
5 thickness. When the channel wall is actuated a sharp heat transfer enhancement is obtained: for a
6 mass flow rate of *1 g/s* the thermal conductance of the virtual prototype is almost the triple than
7 the one of the *200 μm* reference heat exchanger (corresponding thus to an enhancement of
8 approximately *200 %*). For a mass flow rate of *3 g/s* the enhancement is almost *100 %*.

9 The thermal conductance of the virtual prototype appears thus very high. for example, as a
10 comparison point, [8] have developed several prototypes of very compact heat exchangers for the
11 cooling of electronics. They obtained a thermal conductance of *26 W/K* considering a serpentine
12 channel with a mass flow rate of *18 g/s* (leading to a pressure drop of *14 700 Pa*). These thermal
13 conductance is very close from the one obtained with the virtual prototype with a mass flow rate
14 of *3 g/s* (with an imposed zero pressure difference). So, the actuated heat exchanger appears as a
15 good candidate when efficient cooling is needed.

16

17 **CONCLUSION**

18 An experimental setup and a numerical tool have been built in order to analyze
19 hydrothermal performances of heat sink with low diameter channel. For the *1 mm* channel heat
20 exchanger, it was found that the main contribution in the pressure drop is due to the singularities
21 and the tubes upstream and downstream of the heat exchanger, and that the flow is badly
22 distributed in the channel. For the *200 μm* channel, the main contribution in the pressure drop is
23 due to the pressure loss in the channel itself, and the maldistribution is not significant. From heat
24 transfer point of view, the *200 μm* channel heat exchanger allows reaching thermal conductance

1 up to 15 W/K with a very low mass flow rate of 3 g/s . This thermal performance demonstrates
2 that such a liquid cooling heat sink could be efficiently used for the thermal management of
3 electronic chip like microprocessor. Nevertheless, important improvements in the thermo-
4 hydraulic performance could be obtained by optimizing the internal design.

5 Integration of the pumping function within a heat exchanger can be obtained considering
6 dynamic morphing of at least one of the wall of this heat exchanger. In addition, this dynamic
7 morphing may conduct to a significant heat transfer enhancement, making the concept
8 particularly interesting for embedded thermal management systems. A numerical tool has been
9 developed that allows determining the thermo-hydraulic performances of such a heat exchanger.
10 To meet the application constrains, the dynamic deformation has to be realized with a small
11 number of actuators. So, only 3 actuated zones are considered in the present work. It has then
12 been established that:

13 - The mass flow rate is mainly controlled by the frequency and amplitude of the
14 deformation, as well as the gap;

15 - High heat transfer coefficient values can be obtained, up to $20\,000 \text{ W/m}^2\text{K}$;

16 - The corresponding thermal conductance variation according to the mass flow rate is
17 almost twice the one of the $200 \mu\text{m}$ reference static heat exchanger. In addition to the integration
18 of the pumping function within the heat exchanger, important heat transfer enhancement is thus
19 obtained.

20

21 NOMENCLATURE

22

23 A_o relative amplitude, dimensionless

24 C_p specific thermal capacity, $\text{J.kg}^{-1}.\text{K}^{-1}$

25 D_h hydraulic diameter, m

1	f_r	frequency, Hz
2	g	minimum gap of the channel, m
3	h	mean heat transfer coefficient at the heated wall, $\text{W.m}^{-2}.\text{K}^{-1}$
4	$\langle h \rangle$	global heat transfer coefficient at the heated wall, $\text{W.m}^{-2}.\text{K}^{-1}$
5	k_f	fluid thermal conductivity, $\text{W.m}^{-1}.\text{K}^{-1}$
6	L	imprint length of heated zone, m
7	\dot{m}	mass flow rate, kg.s^{-1}
8	q	heat flux, W.m^{-2}
9	P_g	pressure gain in actuated zone, Pa
10	ΔP	pressure difference between outlet-inlet sections, Pa
11	P_p	pumping power, W
12	p	perimeter of the channel passage, m
13	S	exchange surface, m^2
14	t	time, s
15	\bar{T}_{fm}	mean fluid temperature at a given axial position, K
16	$\langle \bar{T}_{fm} \rangle$	mean fluid temperature in the channel, K
17	\bar{T}_w	mean wall temperature on a heated zone, K
18	$\langle \bar{T}_w \rangle$	mean wall temperature in the actuated zone, K
19	$\ \vec{u}\ $	average velocity, m.s^{-1}
20	W	channel width, m

Special characters

21	δ	average distance between walls, m
22	Γ	total solid to fluid heat transfer, W
23	ϕ	volumic heat source, W.m^{-3}
24	ρ	fluid density, kg.m^{-3}
25	λ	wavelength, m
26	ω	number of waves per unit length, m^{-1}
27	μ	dynamic viscosity, $\text{kg.m}^{-1}.\text{s}^{-1}$
28	ξ	pressure drop coefficient, dimensionless
29	τ	period, s

1
2
3
4
5
6
7
8
9
10
11
12
13
14
15
16
17
18
19
20
21
22
23
24

ACKNOWLEDGMENT

This work has been realized in the framework of the CANOPEE project and supported by the "Fond Unique Interministériel (FUI) - 18th call for projects". We gratefully acknowledge contributions from all project partners.

REFERENCES

[1] Léal L., Miscevic M., Lavieille P., Amokrane M., Pigache F., Topin F., Nogarède B., and Tadrist L., An overview of heat transfer enhancement methods and new perspectives: focus on active methods using electroactive materials, *Int. J. Heat Mass Transf.*, vol. 61, pp. 505-524, 2013

[2] Xie X.L., Liu Z.J., He Y.L., and Tao W.Q., Numerical study of laminar heat transfer and pressure characteristics in a water-cooled minichannel heat sink, *Applied Thermal Engineering*, vol. 29, pp. 64-74, 2009

[3] Tullius JF., Vajtai R., and Bayazitoglu Y., A review of cooling in microchannels, *Heat Transfer Engineering*, vol. 32, no. 7-8, pp. 527-541, 2011.

[4] Kheirabadi A.C., and Groulx D., A comparison of numerical strategies for optimal liquid cooled heat sink design, *Proceedings of the ASME 2016 Summer Heat Transfer Conference*, Paper HT2016-7076, July 10-14, Washington DC, USA, 2016.

[5] Kheirabadi A.C., and Groulx D., Cooling of server electronics: a design review of existing technology, *Applied Thermal Engineering*, vol. 105, pp. 622-638, 2016.

[6] Sohail Murshed S.M., and Nieto de Castro C.A., A critical review of traditional and emerging techniques and fluids for electronics cooling, *Renewable and Sustainable Energy Reviews*, vol. 78, pp. 821-833, 2017.

- 1 [7] Habibi Khalaj A., and Halgamuge S.K., A Review on efficient thermal management of air-
2 and liquid-cooled data centers: From chip to the cooling system, *Applied Energy*, vol. 205, pp.
3 1165-1188, 2017.
- 4 [8] Kheirabadi A.C., and Groulx D., Experimental evaluation of a thermal contact liquid cooling
5 system for server electronics, *Applied Thermal Engineering*, vol. 129, pp. 1010-1025, 2018.
- 6 [9] Yang X.H., Tan S.C., Ding Y.J., and Liu J., Flow and thermal modeling and optimization of
7 micro/mini-channel heat sink, *Applied Thermal Engineering*, vol. 117, pp. 289-296, 2017.
- 8 [10] Dixit T., and Ghosh I., Review of micro- and mini-channel heat sinks and heat exchangers
9 for single phase fluids, *Renewable and Sustainable Energy Reviews*, vol. 41, pp. 1298-1311,
10 2015.
- 11 [11] Ghani I.A., Sidik N.A.C., and Kamaruzaman N., Hydrothermal performance of
12 microchannel heat sink: The effect of channel design, *International Journal of Heat and Mass
13 Transfer*, vol. 107, pp. 21-44, 2017.
- 14 [12] Nishimura, T., Ohori, Y., and Kawamura, Y., Flow characteristics in a channel with
15 symmetric wavy wall for steady flow, *Journal of Chemical Eng. of Japan*, Vol., 17, no. 5, pp.
16 466- 471, 1984.
- 17 [13] Nishimura, T., Murakami, S., Arakawa, S., and Kawamura, Y., Flow observations and mass
18 transfer characteristics in symmetrical wavy-walled channels at moderate Reynolds numbers for
19 steady flow, *International Journal of Heat and Mass Transfer*, Vol. 33, no. 5, pp. 835-845, 1990.
- 20 [14] Niceno, N., and Nobile, E., Numerical analysis of fluid flow and heat transfer in periodic
21 wavy channels, *International Journal of Heat and Fluid Flow*, Vol. 22, pp. 156-167, 2001.
- 22 [15] Naphon, P., Effect of wavy plate geometry configurations on the temperature and flow
23 distributions, *International Com. On Heat and Mass Transfer*, Vol. 36, pp. 942-946, 2009.
- 24 [16] Yang C.Y., Yeh C.T., Liu W.C., and Yang B.C., Advanced micro-heat exchangers for high

- 1 heat flux, *Heat transfer Engineering*, vol. 28, no. 8-9, pp. 788-794, 2007.
- 2 [17] Yang C.Y., and Liu W.C, Development of a mini liquid cooling system for high-heat-flux
3 electronic devices, *Heat Transfer Engineering*, vol. 32, no. 7-8, pp. 690-696, 2011.
- 4 [18] Léal, L., Topin, F., Lavieille, P., Tadrist, L., and Miscevic, M., Simultaneous integration,
5 control and enhancement of both fluid flow and heat transfer in small scale heat exchangers: A
6 numerical study, *International Com. onn Heat and Mass Transfer*, vol. 49, pp. 36-40, 2013.
- 7 [19] Kumar, P., Schmidmayer, K., Topin, F., and Miscevic, M., Heat transfer enhancement by
8 dynamic corrugated heat exchanger wall: Numerical study, *Journal of Physics: Conference*
9 *Series*, vol. 745, pp. 32-61, 2016.
- 10 [20] Saeed M., and Kim M.H., Header design approaches for mini-channel heatsinks using
11 analytical and numerical methods, *Applied Thermal Engineering*, vol. 110, pp. 1500-1510, 2017.

12

1
2

Table 1. Presentation of global thermal and flow properties for different mesh sizes for number of time step per period $TS=50$.

BMS	\dot{m} (g/s)	T_w (K)	T_{mf} (K)	$\langle h \rangle$ (W/m ² K)	T_{fi} (K)	T_{fo} (K)
3 mm	1.11	312.51	307.87	13829	301.1	313.8
2 mm	1.10	312.51	307.85	13765	301.1	313.8

3
4
5
6
7

1

Table 2. Presentation of global thermal and flow properties for different time steps for a characteristic mesh size $BMS=2\text{ mm}$

TS (-)	\dot{m} (g/s)	T_w (K)	T_{mf} (K)	$\langle h \rangle$ (W/m ² K)	T_{fi} (K)	T_{fo} (K)
20	1.14	311.7	307.3	14610	300.9	312.6
50	1.10	312.5	307.9	13765	301.1	313.8
75	1.10	312.7	308.0	13615	301.2	314.1
100	1.06	312.8	308.0	13384	301.2	314.2

2

3

4

1
2
3

Table 3. Presentation of operating parameters (wave amplitude and frequency) on mass flow rate, surface and mean fluid temperature difference, heat transfer coefficient, inlet and outlet fluid temperatures.

A (μm)	f_r (Hz)	\dot{m} (g/s)	ΔT_m (K)	$\langle h \rangle$ (W/m ² K)	T_{fi} (K)	T_{fo} (K)
100	10	0.65	5.8	11054	301.75	321.94
100	20	1.31	5.03	12756	301.06	311.94
100	30	1.96	4.56	14071	300.74	308.35
100	40	2.64	4.24	15154	300.60	306.46
100	50	3.34	4.01	16007	300.50	305.32
85	10	0.55	5.43	11808	301.88	325.87
85	20	1.10	4.66	13765	301.12	313.80
85	30	1.68	4.2	15261	300.83	309.63
85	40	2.18	3.91	16381	300.62	307.40
75	10	0.49	5.1	12580	301.94	329.17
75	20	0.97	4.39	14606	301.22	315.65
75	30	1.46	4	16045	300.87	310.79
60	10	0.39	4.62	13879	302.09	336.41
60	20	0.77	4	16067	301.37	319.66
60	30	1.18	3.53	18167	301.00	313.50
60	40	1.62	3.33	19285	300.77	310.16

4
5

1 **List of figure captions**

2
3 **Figure 1.** Picture of the bottom wall of the heat exchanger, made of copper. The two grooves
4 constitute the manifolds.

5 **Figure 2.** Pictures of the heat exchanger after assembly: - left : top view (dug cover) - right : side
6 view. Dimension of the grooved part ($42 \times 49.5 \text{ mm}$; thickness 1 mm (left) and 0.2 mm (right)

7 **Figure 3.** Sketch of the experimental apparatus.

8 **Figure 4.** Cross-section of dynamically corrugated micro-channel. The lower wall is subjected to
9 constant heat flux between x_1 and x_7 , the gap g is the minimum height of the channel. Upper
10 profiles are drawn for 2 different amplitudes and same gap

11 **Figure 5.** Mesh view micro-channel at an arbitrary time. Dimension in the z-direction is
12 magnified 50 times. The bottom wall is uniformly heated below the actuated zone (fine mesh), all
13 other walls are kept adiabatic.

14 **Figure 6.** Experimental and numerical pressure losses as a function of the mass flow rate for the
15 two channel thicknesses.

16 **Figure 7.** Calculated streamlines in the 1 mm channel heat exchanger in adiabatic configuration.
17 The liquid temperature is $20 \text{ }^\circ\text{C}$. Blue: 0 - Red 0.1 m/s .

18 **Figure 8.** Calculated streamlines in the $200 \text{ }\mu\text{m}$ channel heat exchanger in adiabatic
19 configuration. The liquid temperature is $20 \text{ }^\circ\text{C}$. Blue: 0 - Red 0.25 m/s .

20 **Figure 9.** Variation of the pressure loss in the heat exchangers as a function of the mass flow
21 rate. The symbols are the results obtained experimentally; The lines are the results given by Eq.
22 10 with $\sum_i \xi_i = 5$.

23 **Figure 10.** Comparison between regular and singular pressure drops in the 1 mm channel (top)
24 and $200 \text{ }\mu\text{m}$ channel (bottom) heat exchanger. Δp_{tube} represents the pressure drop in the 25 cm
25 upstream and 25 cm downstream tube.

1 **Figure 11.** Instantaneous velocity field: for $A_0=100 \mu m$ and $f_r=10 Hz$. Color range (Blue : 0 -
2 Red 1 m/s). The vertical scale is magnified 100 times. Channel height is 10 μm below center
3 actuator and total length is 7 cm.

4 **Figure 12.** Influence of (top) Frequency for $A_0 = 100 \mu m$ and, (bottom) Amplitude for $f_r=10 Hz$
5 on mass flow rate.

6 **Figure 13.** Influence of gap size on mass flow rate for $A_0 = 100 \mu m$ and $f_r=10 Hz$.

7 **Figure 14.** Variation of the apparent thermal conductance as a function of the mass flow rate for
8 the two channel thicknesses. The same procedure is applied to calculate G (eq. 8) from the
9 experiments and the numerical simulations; the maximum uncertainty is evaluated at 8%.

10 **Figure 15.** Temperature field of the water at mid-height of the 200 μm channel. The inlet
11 temperature is 23.5 °C, the mass flow rate is 1.5 g/s and the heat flux is 62.7 W.

12 **Figure 16.** Temperature field of the water at mid-height of the 1 mm channel. The inlet
13 temperature is 23.5 °C, the mass flow rate is 1.5 g/s and the heat flux is 62.7 W.

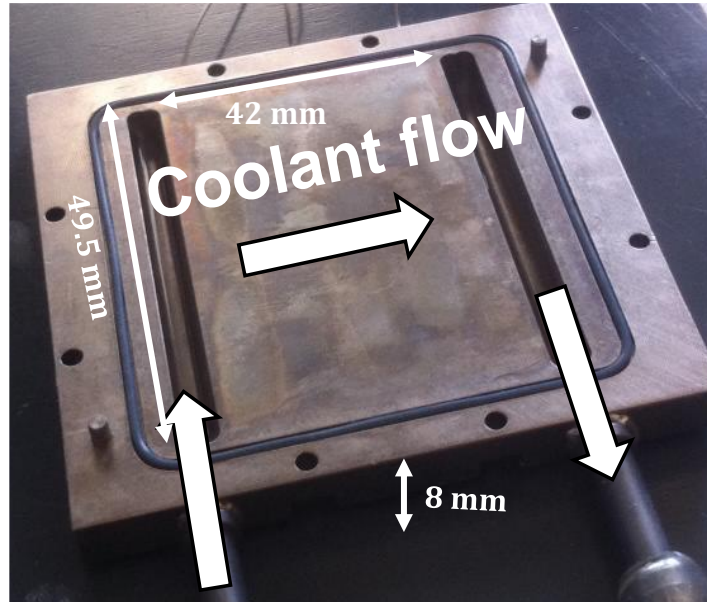
14 **Figure 17.** Instantaneous temperature field for $A_0=100 \mu m$ and $f_r = 10 Hz$. Vertical scale is
15 magnified 100 times. Cold fluid fills the space below 1st actuator (here ascending) with small
16 backflow due to the 2^d actuator "pressing" the fluid on surface (height is about 50 μm). The fluid
17 is mainly driven toward 3rd actuator and outlet.

18 **Figure 18.** Influence of (a) Frequency for $A_0=100 \mu m$ and, (b) Amplitude for $f_r = 10 Hz$ on heat
19 transfer coefficient.

20 **Figure 19.** Thermal conductance as a function of the mass flow rate: comparison between the
21 numerical actuated prototype with $A_0=100 \mu m$, the 200 μm and the 1 mm reference static heat
22 exchangers.

23

1
2
3
4



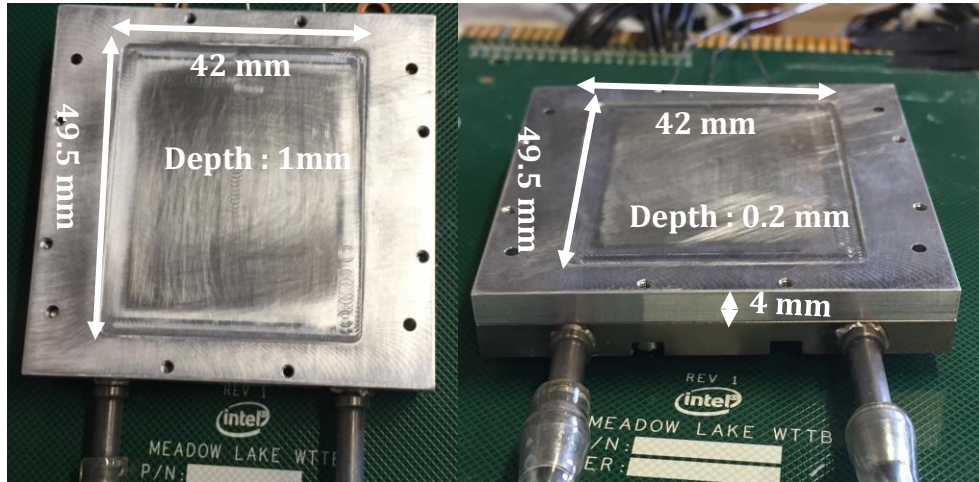
5
6
7
8
9

Figure 1. Picture of the bottom wall of the heat exchanger, made of copper. The two grooves constitute the manifolds.

10
11

1

2



3

4

5 **Figure 2.** Pictures of the heat exchanger after assembly: top cover and bottom plate placed over a
6 CPU Thermal test Vehicle - left : top view (dug cover) - right : side view. Dimension of the
7 grooved part ($42 \times 49.5 \text{ mm}$; thickness 1 mm (left) and 0.2 mm (right)).
8

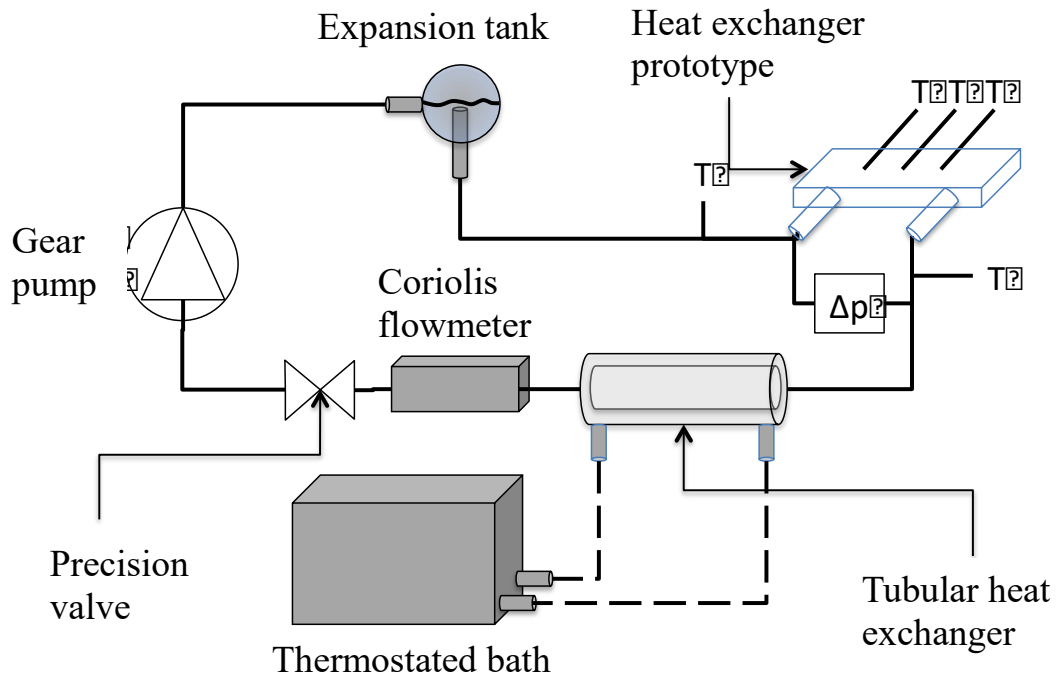
9

10

1

2

3



4

5

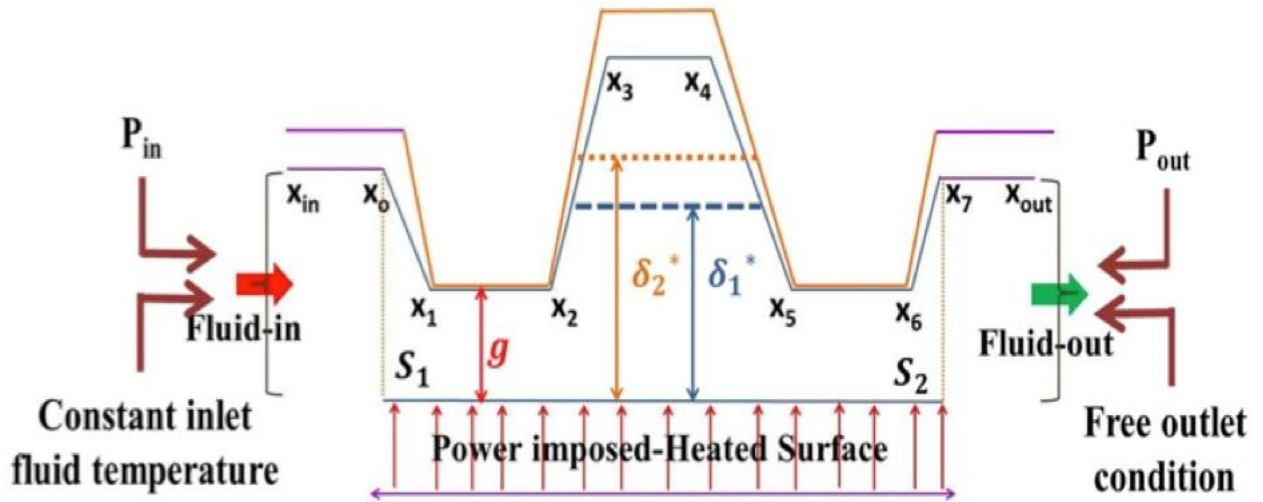
6

7

8

Figure 3. Sketch of the experimental apparatus.

1
2
3
4



5

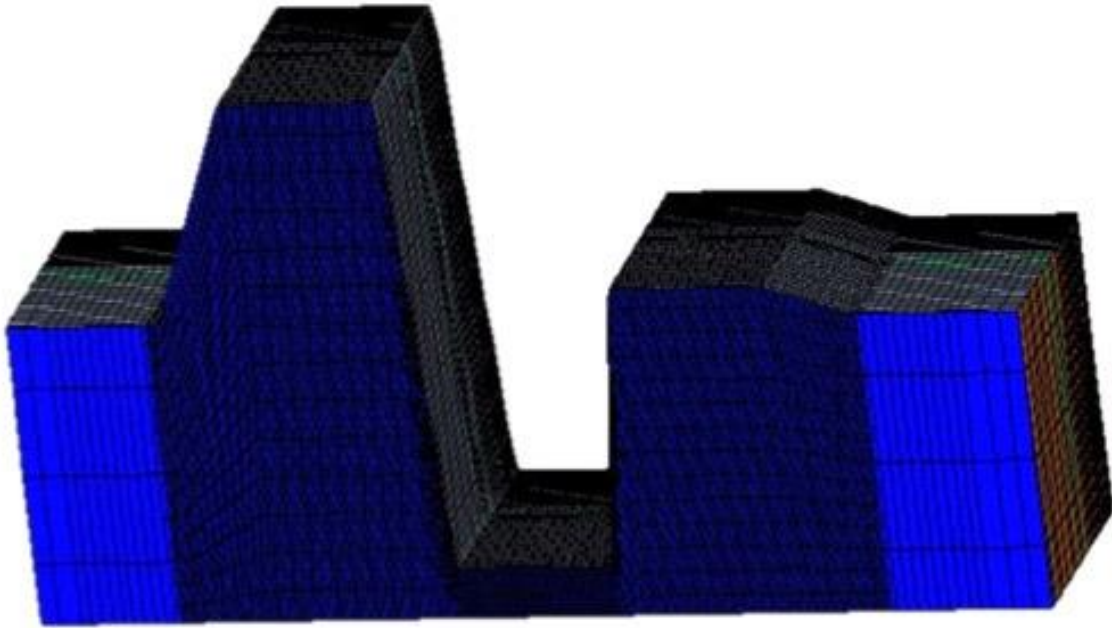
6

7 **Figure 4.** Cross-section of dynamically corrugated micro-channel. The lower wall is subjected to
8 constant heat flux between x_1 and x_7 , the gap g is the minimum height of the channel. Upper
9 profiles are drawn for 2 different amplitudes and same gap

10

11

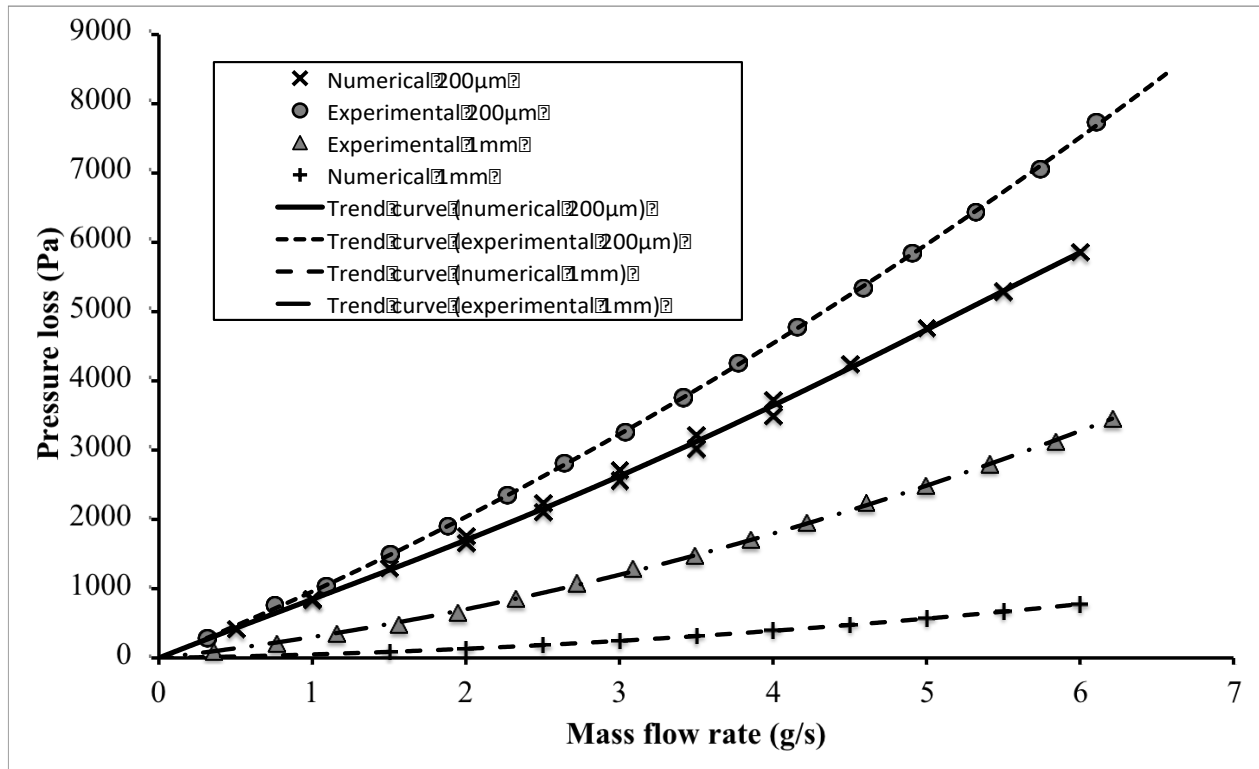
1
2



3
4
5
6
7
8

Figure 5. Mesh view micro-channel at an arbitrary time. Dimension in the z-direction is magnified 50 times. The bottom wall is uniformly heated below the actuated zone (fine mesh), all other walls are kept adiabatic.

1



2

3

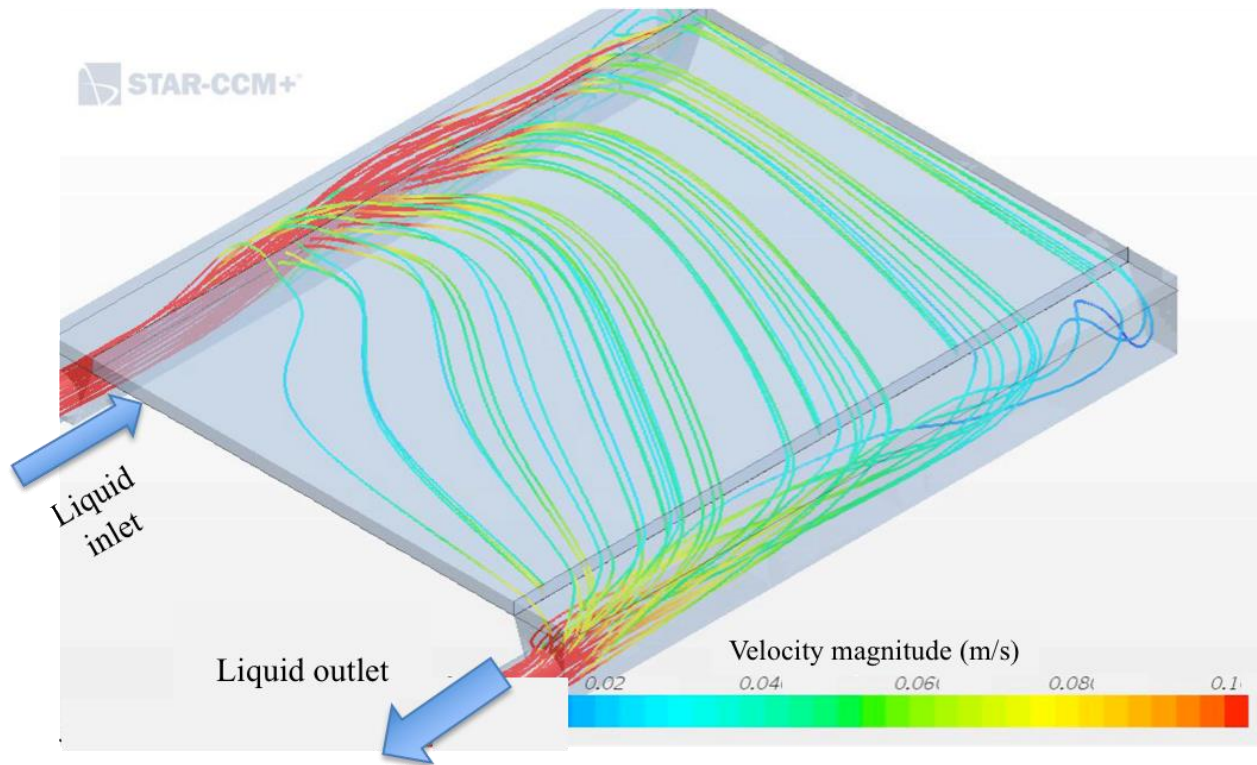
4 **Figure 6.** Experimental and numerical pressure losses as a function of the mass flow rate for the
5 two channel thicknesses.
6

7

1

2

3



4

5

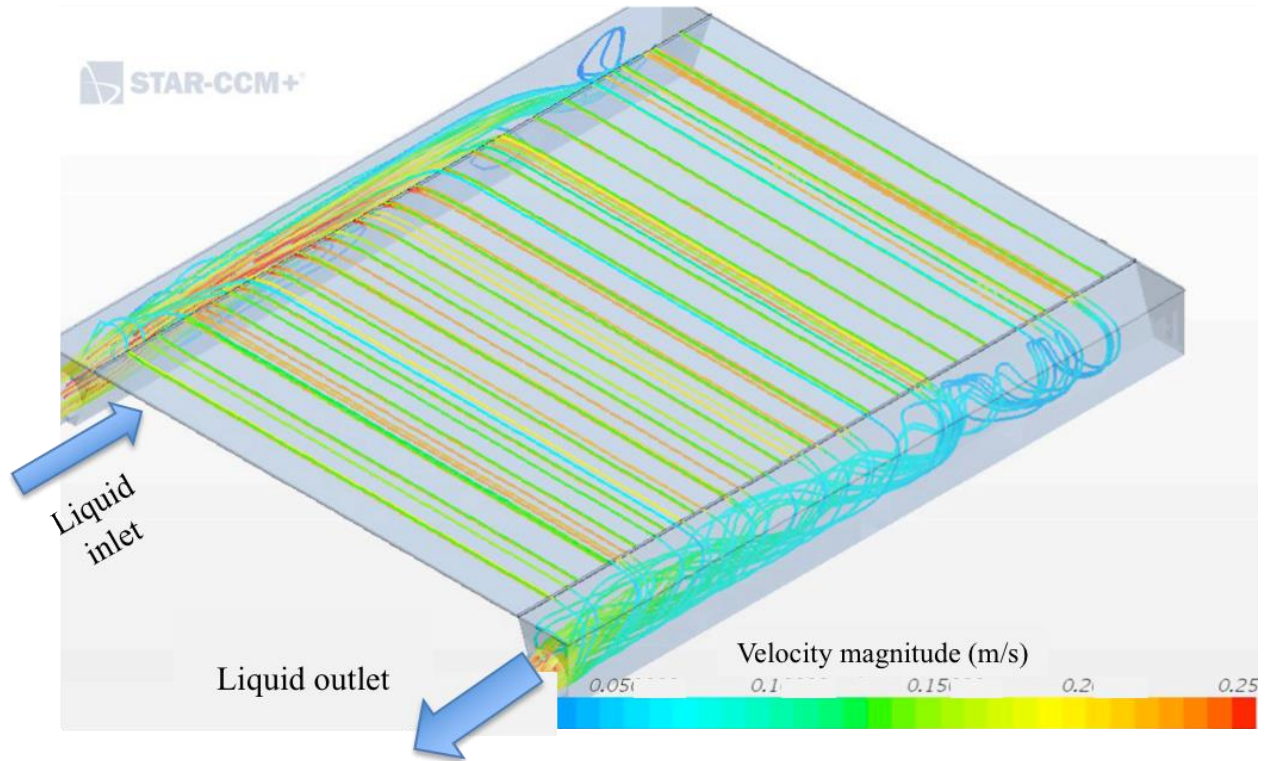
6 **Figure 7.** Calculated streamlines in the 1 mm channel heat exchanger in adiabatic configuration.

7

The liquid temperature is 20 °C. Color range (Blue : 0 - Red 0.1 m/s).

8

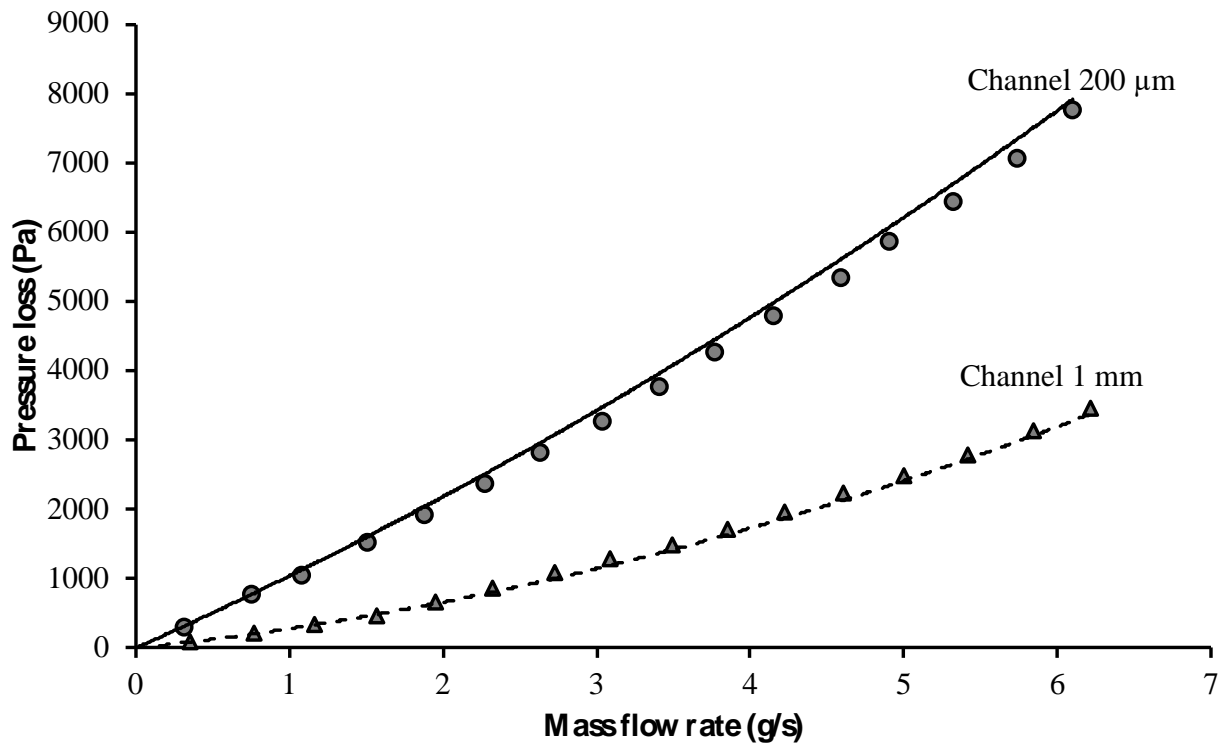
1
2
3



4
5
6
7
8
9
10

Figure 8. Calculated streamlines in the $200\ \mu\text{m}$ channel heat exchanger in adiabatic configuration. The liquid temperature is $20\ \text{°C}$. Color range (Blue : 0 - Red $0.25\ \text{m/s}$).

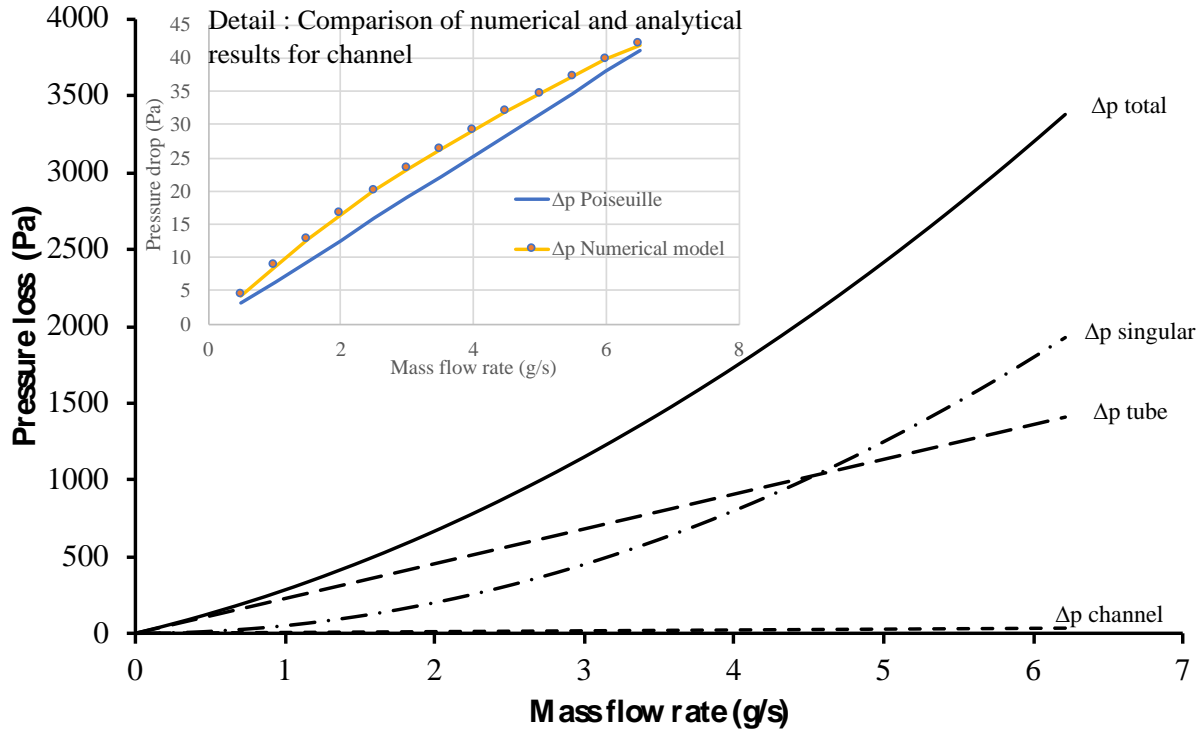
1



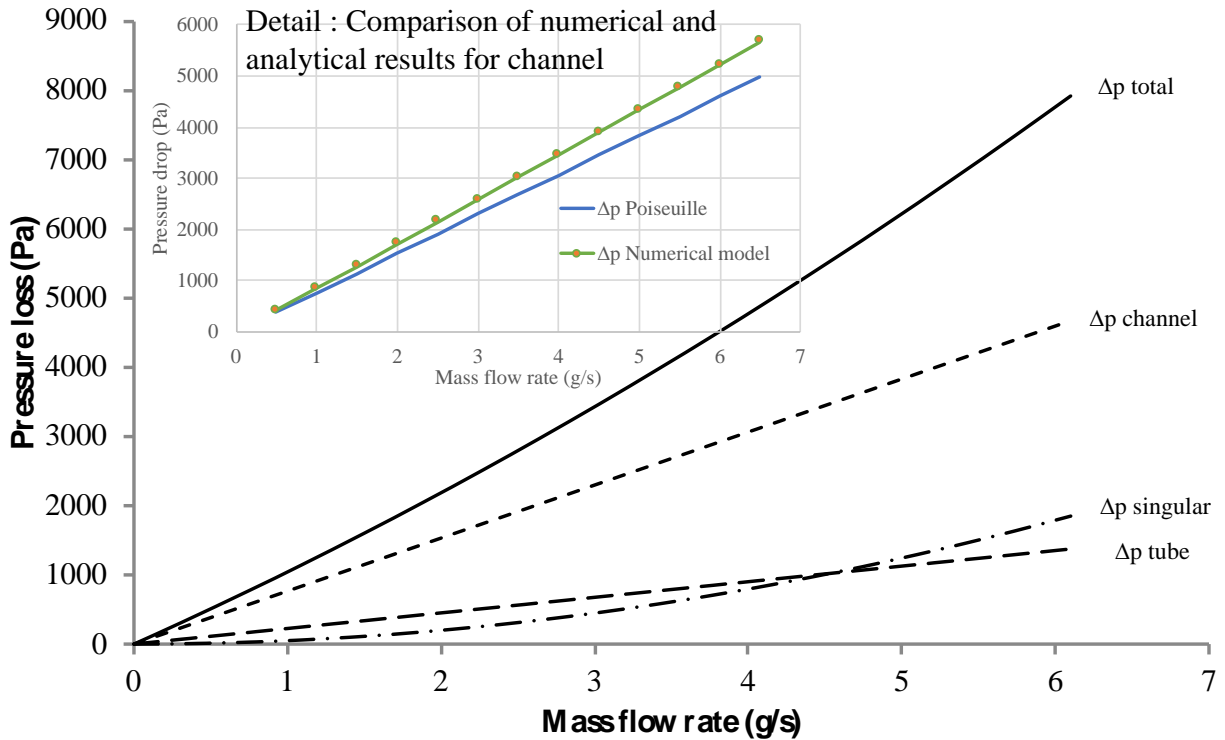
2

3 **Figure 9.** Variation of the pressure loss in the heat exchangers as a function of the mass flow
4 rate. The symbols are the results obtained experimentally; The lines are the results given by Eq.
5 10 with $\sum_i \xi_i = 5$.
6

1



2



3

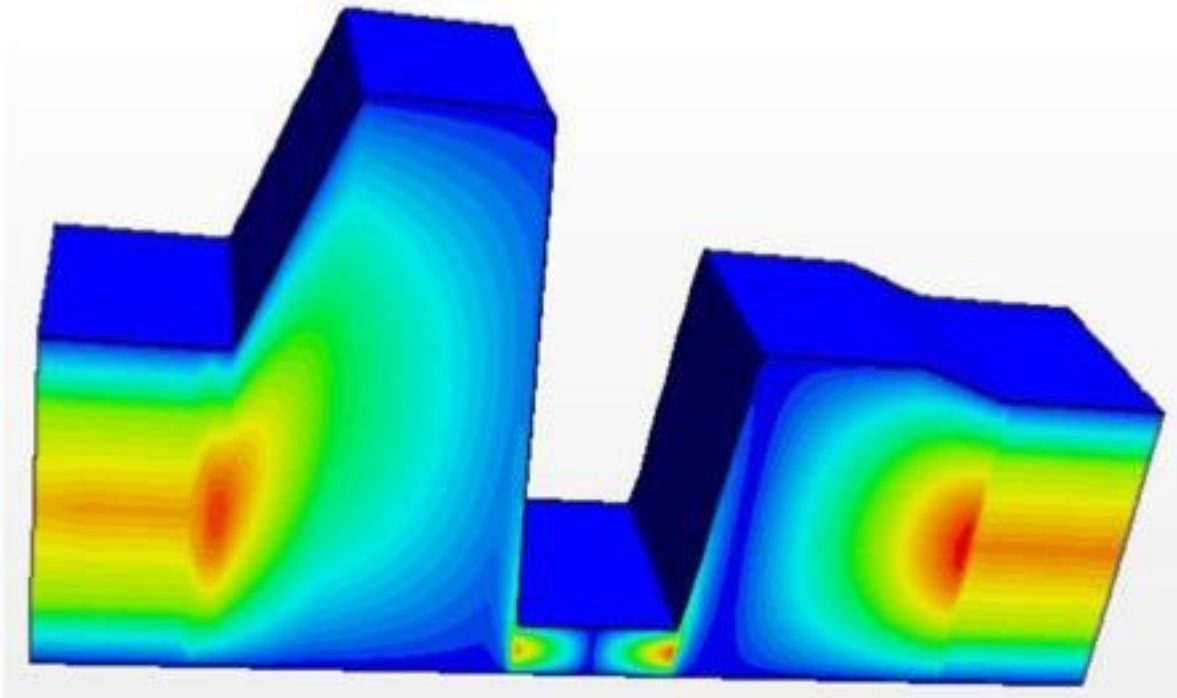
4 **Figure 10.** Comparison between regular and singular pressure drops in the 1 mm channel (top)

5 and 200 μm channel (bottom) heat exchanger. Δp_{tube} represents the pressure drop in the 25 cm

1 upstream and 25 cm downstream tube.

2

3



4

5 **Figure 11.** Instantaneous velocity field: for $A_0=100 \mu m$ and $f_r=10 Hz$. Color range (Blue : 0 -

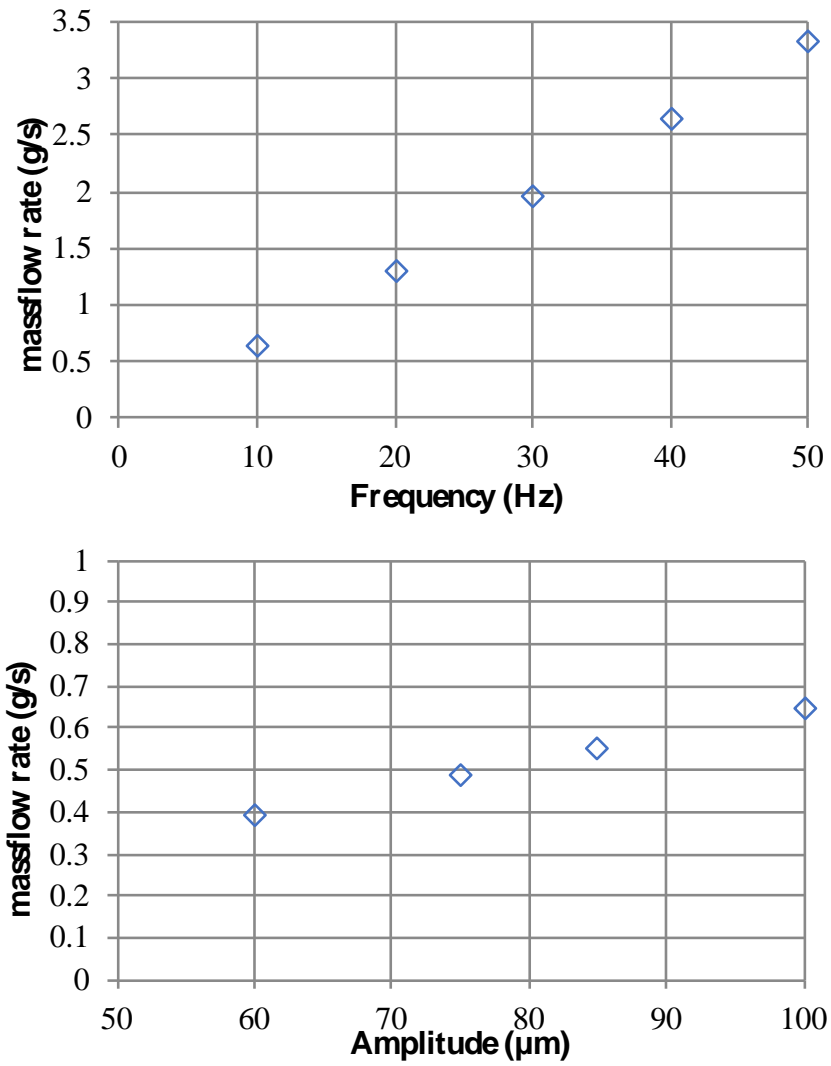
6 Red 1 m/s). The vertical scale is magnified 100 times. Channel height is 10 μm below center

7 actuator and total length is 7 cm.

8

9

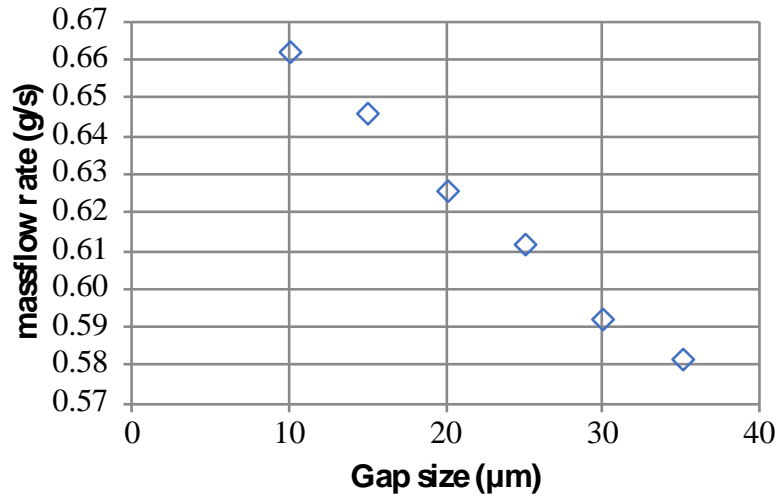
1
2



3
4
5
6
7

Figure 12. Influence of (top) Frequency for $A_0 = 100 \mu m$ and, (bottom) Amplitude for $f_r = 10 Hz$ on mass flow rate.

1



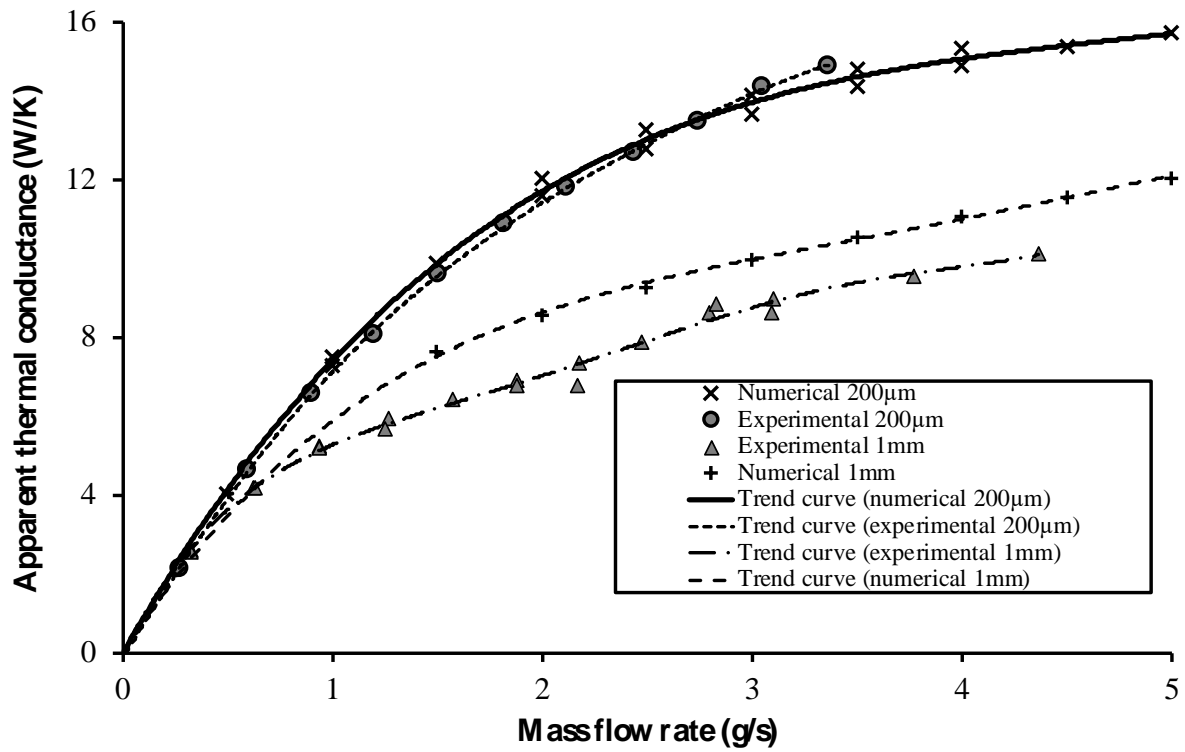
2

3 **Figure 13.** Influence of gap size on mass flow rate for $A_0 = 100 \mu m$ and $f_r = 10 Hz$.

4

5

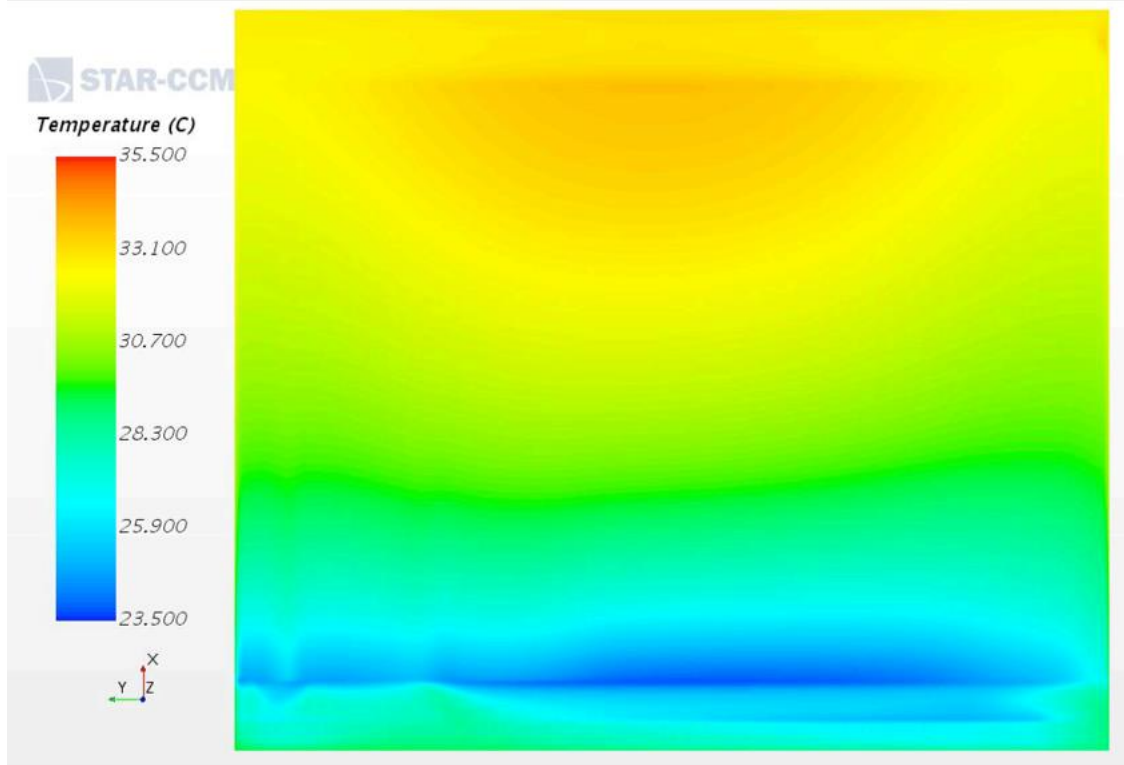
1



2
3

4 **Figure 14.** Variation of the apparent thermal conductance as a function of the mass flow rate for
5 the two channel thicknesses. The same procedure is applied to calculate G (eq. 8) from the
6 experiments and the numerical simulations; the maximum uncertainty is evaluated at 8%.

7
8



1

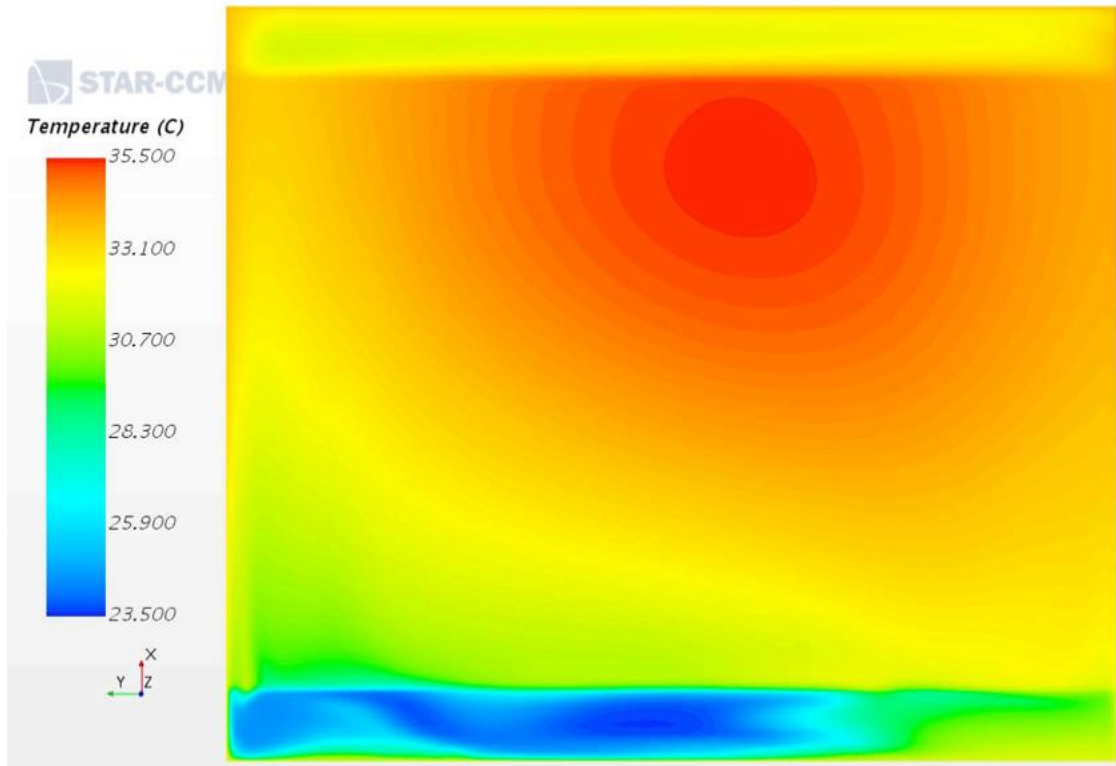
2

Figure 15. Temperature field of the water at mid-height of the $200\ \mu\text{m}$ channel. The inlet temperature is $23.5\ \text{°C}$, the mass flow rate is $1.5\ \text{g/s}$ and the heat flux is $62.7\ \text{W}$.

3

4

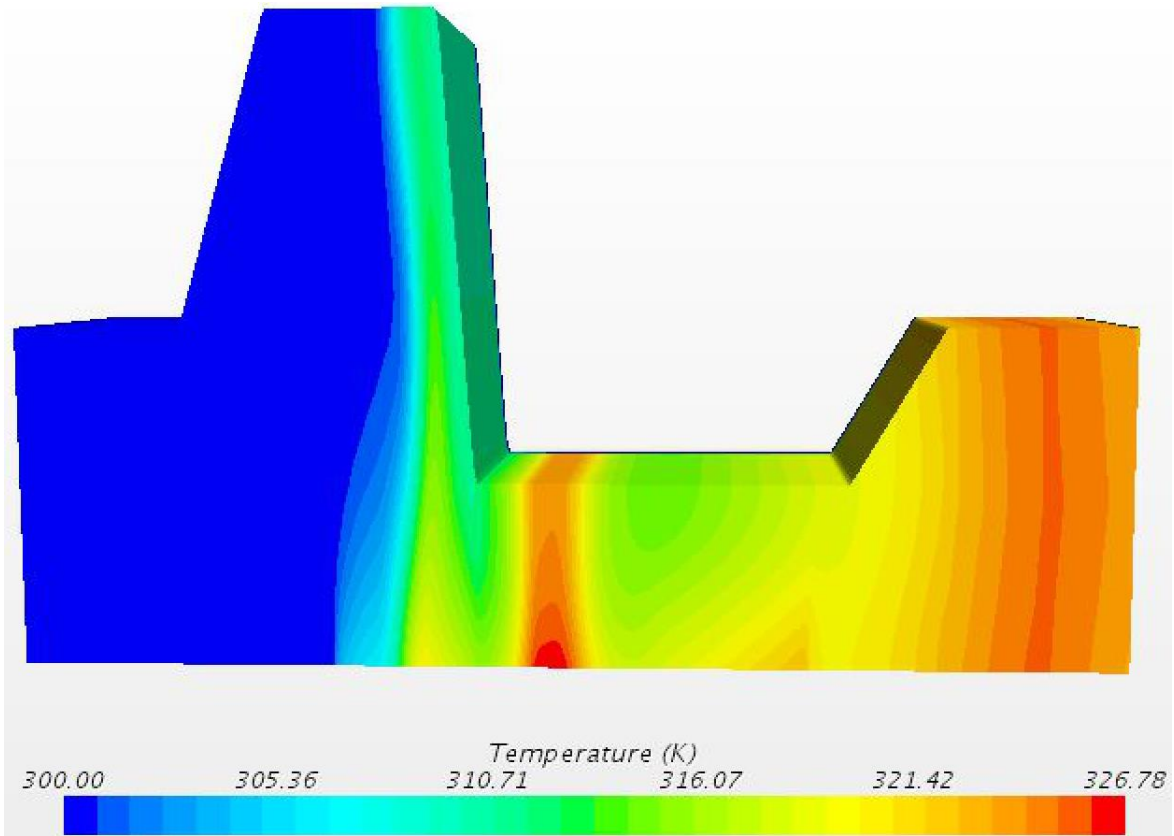
1
2



3
4
5
6
7
8

Figure 16. Temperature field of the water at mid-height of the 1 mm channel. The inlet temperature is $23.5\text{ }^{\circ}\text{C}$, the mass flow rate is 1.5 g/s and the heat flux is 62.7 W .

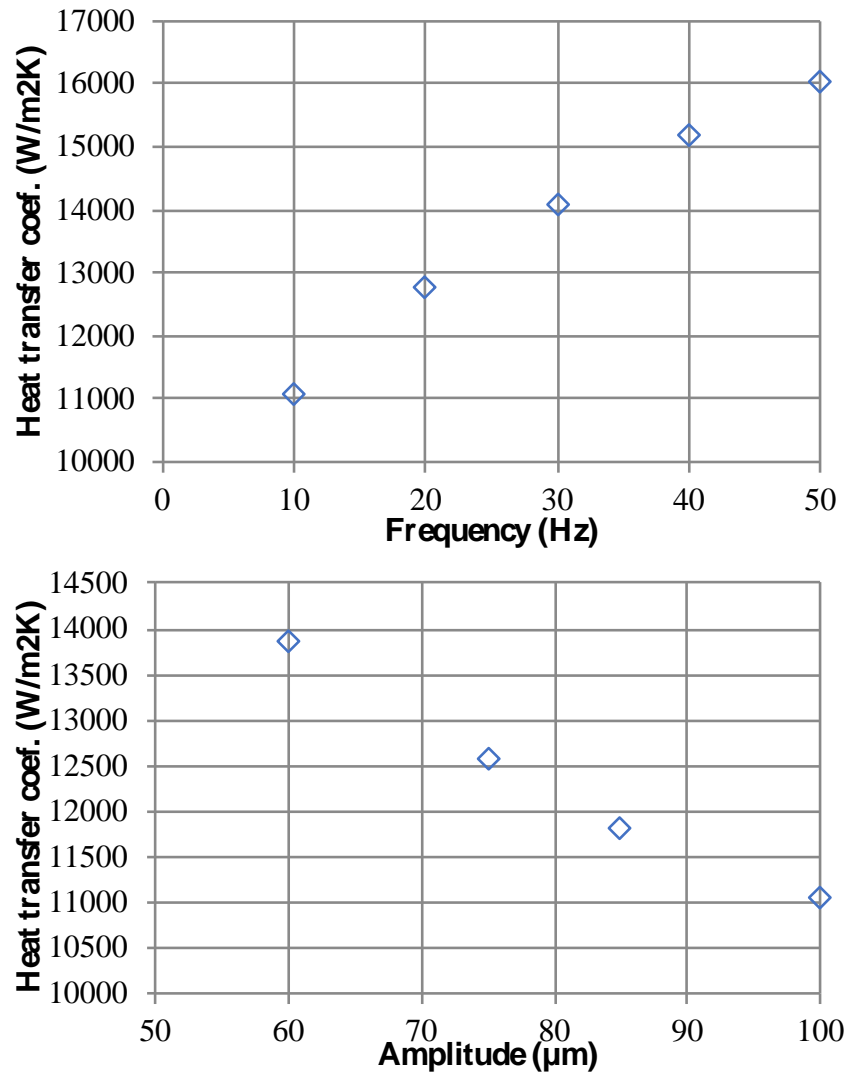
1
2



3
4
5
6
7
8
9
10

Figure 17. Instantaneous temperature field for $A_0=100 \mu\text{m}$ and $f_r = 10 \text{ Hz}$. Vertical scale is magnified 100 times. Cold fluid fills the space below 1st actuator (here ascending) with small backflow due to the 2^d actuator "pressing" the fluid on surface (height is about $50 \mu\text{m}$). The fluid is mainly driven toward 3rd actuator and outlet.

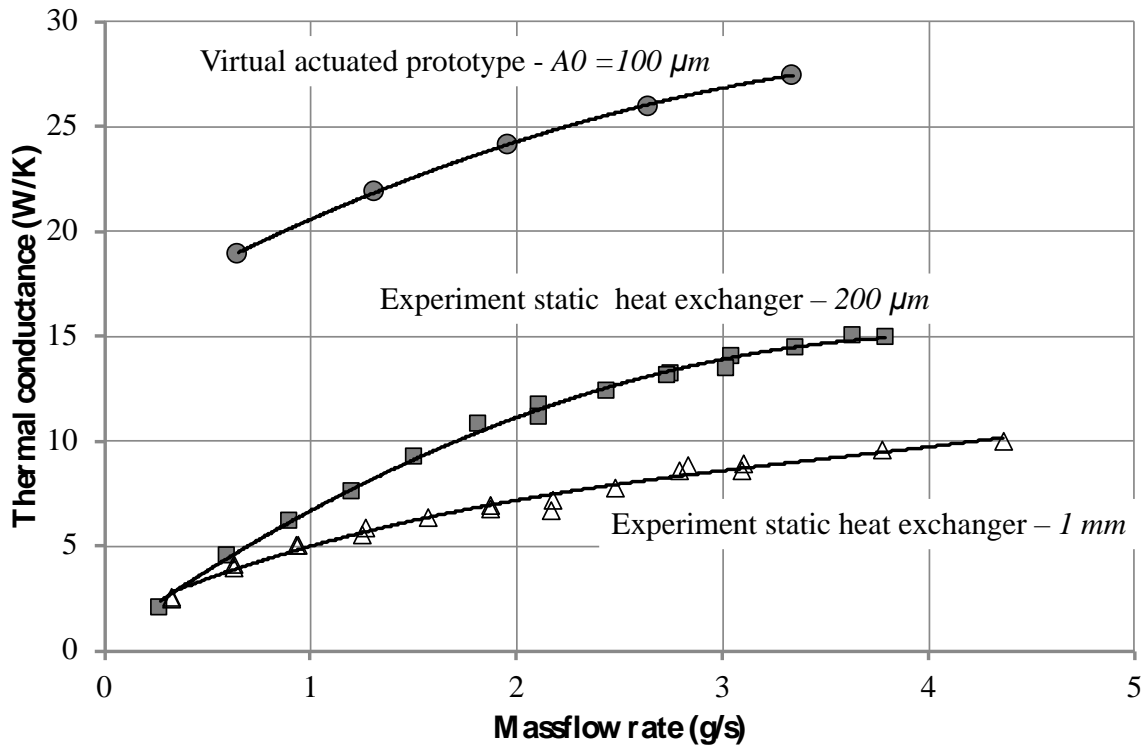
1



2

3 **Figure 18.** Influence of (a) Frequency for $A_0=100 \mu m$ and, (b) Amplitude for $f_r = 10 Hz$ on heat
4 transfer coefficient.

5



1
 2 **Figure 19.** Thermal conductance as a function of the mass flow rate: comparison between the
 3 numerical actuated prototype with $A_0=100 \mu m$, the $200 \mu m$ and the $1 mm$ reference static heat
 4 exchangers.

5
 6



Julien Michel Fontaine graduated in electrical engineering and automatics from the engineering school ENSEEIHT at Toulouse, France, in 2014. He is currently a Ph.D. student at the Federal University Toulouse Midi-Pyrénées, France. The field of his research is piezoelectric actuation dedicated to micropumping and the improvement of heat transfer.



Prashant Kumar graduated in Computational Fluid Mechanics from Trinity college in Dublin, Ireland, in 2010. He obtained his Ph.D. entitled “Investigation of Kelvin-like solid foams for potential engineering applications: An attractive set of geometrical and thermo-hydraulic properties” in 2014 from Aix-Marseille Université, France. He then becomes involved in CFD analysis of dynamically deformed heat exchangers in IUSTI until 2017. He then joined ESILON-Alcen in Toulouse.



Francois Pigache is an associate professor at LAPLACE, Toulouse University, France, since 2006. Before joining the LAPLACE, he obtained his Ph.D. in 2005 from the Université Sciences et technologies de Lille, France. He is involved in research in the areas of multiphysics modelling, the optimization of the piezoelectric transformers, and alternative applications of the electroactive materials for the surface functionalization.



Pascal Lavieille has been an assistant professor in the LAPLACE Laboratory, University Paul Sabatier of Toulouse, France since 2002. He obtained his Ph.D. in 2001 from the University H. Poincaré in Nancy, France. He is a specialist in optical diagnostic for the determination of temperatures fields and measurement of film thickness. His research interests are focused on phase change (condensation, boiling, capillary phenomena, wettability), and two-phase cooling systems.



Frédéric Topin is an associate professor at IUSTI, Aix-Marseille Université, France, since 1996. He obtained his Ph.D. in 1995 from the Université de Provence in Marseille, France. He is involved in research in the areas of transport phenomena in porous media (Structure - Flows/Transfers - Reactions), dynamic fluid structure interaction, pore scale modeling of flow and phase change in solid foams and coupled phenomena such as bio fuel cells or stability of superconductor cables.



Marc Miscovic is an associate professor at LAPLACE, Toulouse University, France, since 1999. Prior coming to LAPLACE, he obtained his Ph.D. in 1997 from the Université de Provence in Marseille, France. He is involved in research in the areas of active method of heat transfer enhancement, phase change in micro channels and microgravity (condensation, boiling, capillary phenomena, wettability), and two-phase cooling systems.